Tick extracellular vesicles undermine epidermal wound healing during hematophagy

Liron Marnin[1£], Luisa M. Valencia[1£], Haikel N. Bogale[2†], Hanna J. Laukaitis-Yousey[1], Agustin Rolandelli[1¥], Camila Rodrigues Ferraz[1], Anya J. O'Neal[1‡], Axel D. Schmitter-Sánchez[3,4,5], Emily Bencosme Cuevas[6], Thu-Thuy Nguyen[6], Brenda Leal-Galvan[7], David M. Rickert[1], M. Tays Mendes[1§#], Sourabh Samaddar[1], L. Rainer Butler[1α], Nisha Singh[1β], Francy E. Cabrera Paz[1], Jonathan D. Oliver[8], Julie M Jameson[9], Ulrike G. Munderloh[10], Adela S. Oliva Chávez[7€], Albert Mulenga[6], Sangbum Park[3,4,5], David Serre[1,2], and Joao H.F. Pedra[1*].

Affiliations:

[1]Department of Microbiology and Immunology, University of Maryland School of Medicine, Baltimore, MD, USA.
[2]Institute for Genome Sciences, University of Maryland School of Medicine, Baltimore, MD, USA.
[3]Division of Dermatology, Department of Medicine, College of Human Medicine, Michigan State University, East Lansing, MI, USA.
[4]Department of Pharmacology and Toxicology, College of Human Medicine, Michigan State University, East Lansing, MI, USA.
[5]Institute for Quantitative Health Science & Engineering, Michigan State University, East Lansing, MI, USA.
[6]Department of Veterinary Pathobiology, School of Veterinary Medicine and Biomedical Sciences, Texas A&M University, College Station, TX, USA.
[7]Department of Entomology, Texas A&M University, College Station, TX, USA.
[8]Division of Environmental Health Sciences, School of Public Health, University of Minnesota, Minneapolis, MN, USA.
[9]Department of Biology, California State University San Marcos, San Marcos, CA, USA.
[10]Department of Entomology, University of Minnesota, Minneapolis, MN, USA.

[†]Present address: Rancho BioSciences, San Diego, CA, USA.
[¥]Present address: University Lille, CNRS, INSERM, CHU Lille, Institut Pasteur de Lille, U1019-UMR9017-CIIL-Center for Infection and Immunity of Lille, Lille, France.
[‡]Present address: Immunology Program, Memorial Sloan Kettering Cancer Center, New York, NY, USA.
[§]Present address: Ribeirão Preto Medical School, University of São Paulo, Ribeirão Preto, Brazil.
[#]Present address: Fiocruz-Bi-Institutional Translational Medicine Project, Ribeirão Preto, Brazil.
[α]Present address: Department of Genetics, Blavatnik Institute, Harvard Medical School, Boston, MA, USA.
[β]Present address: Department of Biotechnology, School of Energy Technology, Pandit Deendayal Energy University; Knowledge Corridor, Gandhinagar, Gujarat, India
[€]Present address: Department of Entomology, University of Wisconsin, Madison, WI, USA

[£]Equal contribution

*Corresponding author: jpedra@som.umaryland.edu

Keywords: Arthropod Vectors; Ticks; Tick-Borne Diseases; Skin; Wound Healing

Abstract

Wound healing has been extensively studied through the lens of inflammatory disorders and cancer, but limited attention has been given to hematophagy and arthropod-borne diseases. Hematophagous ectoparasites, including ticks, subvert the wound healing response to maintain prolonged attachment and facilitate blood-feeding. Here, we unveil a strategy by which extracellular vesicles (EVs) ensure blood-feeding and arthropod survival in three medically relevant tick species. We demonstrate through single cell RNA sequencing and murine genetics that wildtype animals infested with EV-deficient *Ixodes scapularis* display a unique population of keratinocytes with an overrepresentation of pathways connected to wound healing. Tick feeding affected keratinocyte proliferation in a density-dependent manner, which relied on EVs and dendritic epidermal T cells (DETCs). This occurrence was linked to phosphoinositide 3-kinase activity, keratinocyte growth factor (KGF) and transforming growth factor β (TGF-β) levels. Collectively, we uncovered a strategy employed by a blood-feeding arthropod that impairs the integrity of the epithelial barrier, contributing to ectoparasite fitness.

Introduction

Ectoparasitic arthropods obtain their nourishment by feeding on a vertebrate host, providing an avenue for microbial transmission during hematophagy (Sonenshine & Roe, 2014). In North America, tick encounters account for approximately 77% of all arthropod-borne diseases, with most interactions attributed to *Ixodes*, *Amblyomma* and *Dermacentor* species (Eisen, 2022; Rosenberg et al., 2018). Notably, *Ixodes scapularis* is an arthropod vector of several human illnesses, including Lyme disease (Eisen, 2022). The Lone star tick *Amblyomma americanum* transmits bacteria that cause ehrlichiosis, while the American dog tick *Dermacentor variabilis* and *Dermacentor andersoni* carry pathogens associated with Rocky Mountain spotted fever and tularemia (Eisen, 2022; Rosenberg et al., 2018).

The unique microenvironment generated at the skin interface during a tick bite is conducive to arthropod hematophagy and pathogen transmission (Wikel, 2013). Unlike other blood-feeding arthropods, the development of hard ticks incorporates a series of events which necessitate long-term attachment to the skin (Sonenshine & Roe, 2014). This prolonged disruption of the host physical barrier poses a new challenge for tick survival as defense mechanisms are engaged. Tick saliva has been shown to be critical to subvert inflammation, blood coagulation, and nociception and antagonizes host immunity to enable attachment to the skin (Esteves et al., 2017; Francischetti et al., 2009; Kazimirova & Stibraniova, 2013; Kotal et al., 2015; Kotsyfakis et al., 2007; Kramer et al., 2011; Poole et al., 2013; Ribeiro et al., 1992; Ribeiro et al., 1985; Ribeiro et al., 1988; Simo et al., 2017; Valenzuela et al., 2002). Observations across various species further demonstrate a conserved ability whereby tick effectors perturb pro-inflammatory mediators responding to ectoparasite feeding (Bakshi et al., 2019; Dickinson et al., 1976; Esteves et al., 2017; Karim & Ribeiro, 2015). Such antagonism of host responses has been implicated in the dissemination and persistence of vector-borne pathogens (Chen et al., 2014; Kotsyfakis et al., 2010; Oliva Chávez et al., 2021).

As the largest organ in the body, the skin serves as the first line of defense against arthropod infestation and pathogen transmission (Eyerich et al., 2018; Glatz et al., 2017; Kabashima et al., 2019). The skin is comprised of three primary layers: the outermost epidermis, the underlying dermis, and the hypodermis or subcutaneous fat (Eyerich et al., 2018). The complex architecture and specialized cell populations comprising the skin affords the mammalian host a protective barrier against environmental and microbial threats, in addition to aiding in thermoregulation and prevention of trans-epidermal water loss (Kabashima et al., 2019; Proksch et al., 2008). During injury, such as laceration of the skin by a tick hypostome, various immune and sentinel cells are activated and release soluble factors that prompts the highly complex and intricate process of wound healing (Singer & Clark, 1999). Proper wound healing requires a high degree of coordination to orchestrate a response to an insult, which is broadly comprised of four overlapping stages: hemostasis, inflammation, proliferation, and tissue remodeling (Peña & Martin, 2024).

Little attention has been paid to the latter phases of skin healing during tick hematophagy, including proliferation, which drives the process of re-epithelialization. Re-epithelialization, which is largely dependent on the proliferation of keratinocytes, culminates in the regeneration of the epidermal-dermal junction and restoration of barrier integrity (Pastar et al., 2014; Rousselle et al., 2019). Keratinocytes function as structural cells which serve as the outermost layer in mammals (Pastar et al., 2014; Rousselle et al., 2019). Keratinocytes have also been recognized as sentinels, facilitating crosstalk with immune cells, and partaking in the initiation of the wound healing response upon injury (Piipponen et al., 2020). Dysfunction in keratinocyte-mediated closure has been reported in chronic wounds indicating their crucial role in skin homeostasis (Pastar et al., 2014; Wikramanayake et al., 2014).

The current paradigm at the tick-skin interface is that salivary molecules are deposited within the dermis during feeding, where they actively regulate the cutaneous response to an insult (Bernard et al., 2020; Wikel, 2013). The impact of tick feeding on the epidermis, which

113 interfaces with the external environment, has been mostly neglected. The significance of the
114 epidermis in countering tick infestation was documented in the late 1970s wherein Langerhans
115 cells were shown to respond to salivary antigens (Allen et al., 1979). We also implicated
116 extracellular vesicles (EVs) originating from the tick *I. scapularis* in promoting tick fitness and
117 generating distinct outcomes of pathogen transmission in mammals. This mechanism was
118 accomplished through the tick SNARE protein Vamp33 and epidermal γδ T cells (Oliva Chávez
119 et al., 2021).

120 In this article, we combined single cell RNA sequencing (scRNA-seq), murine genetics,
121 intravital microscopy and flow cytometry to reveal that tick EVs disrupt intraepithelial
122 homeostasis. We discovered a unique population of keratinocytes in wildtype animals with an
123 overrepresentation of pathways connected to wound healing during a bite from EV-deficient
124 ticks. We further underpinned this biological network by demonstrating that tick EVs impacted
125 epithelial proliferation through the disruption of phosphoinositide 3-kinase (PI3K) activity,
126 keratinocyte growth factor (KGF) and transforming growth factor β (TGF-β). Collectively, we
127 illustrate a tick-induced interference of wound healing via the skin epidermis, contributing to the
128 process of arthropod hematophagy.

Results

Tick extracellular vesicles enable arthropod fitness. We previously observed that EVs derived from *I. scapularis* enabled hematophagy (Oliva Chávez et al., 2021). We sought to corroborate our findings in other tick species of public health importance and assess the impact of EVs on arthropod fitness. Total genetic ablation in ticks remains beyond current technical capabilities because editing through clustered regularly interspaced short palindromic repeats (CRISPR) has only been applied to score morphological phenotypes, but not signaling pathways (Sharma et al., 2022). Thus, we silenced the expression of the *vesicle associated membrane protein 33* (*vamp33*) through RNA interference (RNAi) to study the effect of tick EVs.

We designated arthropods that had reduced *vamp33* gene expression as si*V33*, EV-deficient ticks, and the scramble control treatment as sc*V33*, EV-sufficient ticks. Si*V33* and sc*V33* microinjected nymphs were placed on C57BL/6 mice and allowed to feed for 3 days (Fig. 1A). On day 3, *I. scapularis* were assessed for efficiency of *vamp33* silencing, attachment, and collected for weight and post-feeding survival (Fig. 1B-E). We observed a statistically significant difference in attachment between si*V33* and sc*V33* nymphs (Fig. 1C) compared to our previous evaluation (Oliva Chávez et al., 2021). Diminished feeding was also measured for EV-deficient ticks as demonstrated by a 53% reduction in tick weight (Fig. 1D). Interrupted feeding in *I. scapularis* led to reduced survival post-detachment (Fig. 1E). An EV-associated fitness cost upon *vamp33* silencing was observed in all three clinically relevant tick species (Fig. 1B-M). A notable exception was the lack of phenotypic differences in attachment for *A. americanum* compared to *I. scapularis* and *D. variabilis* (Fig. 1C, G, and K). Collectively, these findings offer the prospect of a cross-species integrated management for mammalian infestation despite the distinct tick phylogeny.

Tick EVs alter epidermal immune surveillance. Recently, we reported that tick EVs within saliva affect the frequency of dendritic epidermal T cells (DETC) and alter the cytokine

and chemokine milieu of the skin (Oliva Chávez et al., 2021). DETC surveillance of keratinocytes via various cell surface receptors is critical in a wounding response, leading to the activation and recruitment of immune cells, stimulation of keratinocytes for proliferation and survival, and anti-microbial responses (Jameson et al., 2002; Jameson et al., 2004; Keyes et al., 2016; Macleod & Havran, 2011; Sharp et al., 2005) (Fig. 2A). This crosstalk and surveillance between DETC and keratinocytes led us to reason that tick EVs might not solely impact DETCs, but also likely influence the most abundant epidermal cell, the keratinocyte. Hence, we allowed EV-deficient (si*V33*) and EV-sufficient (sc*V33*) *I. scapularis* nymphs to feed on mice for 3 days and collected the skin biopsy for flow cytometry evaluation (Supplementary Fig. 1). We observed a decrease in DETC frequency during sc*V33* tick feeding on mice compared to naïve skin (Fig. 2B). Conversely, DETC frequency remained at homeostatic levels after impairment of tick EVs (si*V33*) and ectoparasite feeding on murine animals (Fig. 2B).

DETCs exhibit a dendritic shape that allows for continuous surveillance of neighboring keratinocytes through various receptor-ligand interactions (Jameson et al., 2002; Witherden et al., 2012) (Fig. 2A). Upon tissue damage, stressed keratinocytes upregulate ligands and antigens that stimulate DETCs in a non-major histocompatibility complex (MHC)-restricted manner (Havran et al., 1991). Activated DETCs will then alter their morphology by retracting dendrites and assuming a rounded configuration to facilitate migration to the site of injury (Jameson et al., 2002; Nielsen et al., 2017). To determine the possible role of keratinocytes during tick feeding, we assessed the DETC co-stimulatory markers that facilitate immune surveillance. We observed an elevated co-receptor frequency among DETCs found at the skin interface where EV-sufficient ticks fed on mice, including the junctional adhesion molecule-like (JAML) and the C-type lectin-receptor NKG2D (also known as KLRK1) (Girardi et al., 2001; Whang et al., 2009) (Fig. 2C-D). Similar findings were also observed for the activation markers CD69 and CD25 (Fig. 2E-F). Conversely, JAML, NKG2D, CD69 and CD25 were not upregulated in the bite of EV-deficient ticks during murine feeding (Fig. 2C-F).

Morphologically, the hallmark of DETC activation is the conversion of a dendritic to a rounded morphology that facilitates intraepidermal migration, a phenomenon that is partially regulated by CD100 signaling (Thelen & Witherden, 2020; Witherden et al., 2012). To capture morphological changes in DETCs, we employed intravital microscopy of EV injection into the ear of a triple-reporter mouse model. Intravital microscopy of EV injection into the ear of this mouse model revealed that tick EVs did not promote rounding of DETCs, as compared to the positive control cytochalasin D (Fig. 2G). Supporting epidermal intravital imaging findings, expression of CD100 was not altered during a tick bite regardless of the EV status (Fig. 2H). Altogether, these findings provided evidence that tick EVs functionally alter immune surveillance of the epidermal niche by DETCs.

ScRNA-seq characterization of epidermal cells during tick feeding. Given the functional perturbations in DETCs during tick feeding, and the well documented importance of the DETC-keratinocyte crosstalk during wounding, we hypothesized that the epidermal healing circuitry is likely being altered during tick feeding. To evaluate this hypothesis, we utilized scRNA-seq to analyze the impact of tick EVs on the epidermal immune environment in both DETC-deficient (FVB-Tac) and DETC-sufficient (FVB-Jax) mice three days after tick feeding. FVB-Tac mice are depleted of functional DETCs due to a failure of thymic selection because of a natural mutation of the *skint1* gene (Barbee et al., 2011; Boyden et al., 2008; Lewis et al., 2006). Skin punch biopsies were obtained from the bite site, and the epidermis was enzymatically separated from the dermis. Live cells were sorted by fluorescence activation and libraries were generated for Illumina sequencing (Fig. 3A).

Our analysis encompassed approximately 20,640 cells, with an average of 88,027 reads. Our initial investigation resulted in 23 clusters (Supplementary Dataset 1). Next, we applied a fixed threshold to retain cells with more than 2500 UMIs (Supplementary Fig. 2A-B) and applied the DoubletFinder R package to predict doublets (Supplementary Fig. 2C-D). We

identified 10 distinct groups of cells through an analysis of marker genes within each cluster relative to the entire dataset (Supplementary Dataset 2). Keratinocytes, T cells, fibroblasts and endothelial cells were observed in our scRNA-seq results (Supplementary Fig. 2D). The presence of dermal clusters in our study was likely due to an incomplete epidermal-dermal border separation during the enzymatic dissociation of skin biopsies. Thus, we subjected keratinocytes, T cells, and antigen-presenting cells (APCs) to a second round of clustering (Supplementary Dataset 3). This dataset revealed a total of 8 clusters visualized in t-distributed stochastic neighbor embedding (t-SNE) (Fig. 3B) for a total of 5,172 total cells with a median UMI count of 13,910 per cell.

Throughout the process of differentiation, keratinocytes express different types of keratins, including keratins (*Krt*) *1*, *5*, *10*, and *14* (Fuchs, 1993). Elevated levels of *Krt5* and *Krt14* expression enabled the recognition of undifferentiated cells residing within the basal layer of the epidermis (Fig. 3C, Supplementary Dataset 4). *Krt1*, *Krt10*, and *Involucrin* were used to discern early and late-stage differentiation of keratinocytes (Fig. 3C, Supplementary Fig. 3, Supplementary Dataset 4). APCs and T cells were identified by the T cell receptor alpha constant (*Trac*), the T cell receptor delta constant (*Trdc*), and the histocompatibility class II antigen (*H2-Aa*) (Supplementary Dataset 3, Supplementary Table 2). The mouse epidermis harbors hair follicles with distinct physiological functions (Joost et al., 2018; Joost et al., 2016). Our dataset only accounted for compartments in anatomical proximity to the epidermis (Supplementary Fig. 4, Supplementary Table 2).

We then determined the percent distribution of interfollicular epidermal cells per treatment. In the skin biopsy where ticks fed on immune intact mice (FVB-Jax sc*V33* and FVB Jax si*V33*), we observed a decrease in keratinocytes and an overrepresentation of T cells and APCs compared to the naïve skin (Supplementary Fig. 5A-B, Supplementary Dataset 5). A similar effect was not observed when ticks fed on the skin of DETC-deficient mice, presumably due to the diminished wound healing capacity in FVB-Tac animals (Keyes et al., 2016). We

confirmed the depletion of DETCs in the epidermis of FVB-Tac mice. Gene expression of *Trdv4* in the T cell cluster, which encodes for the receptor Vδ1 in DETCs, was reduced in FVB-Tac compared to the FVB-Jax mouse strain (Supplementary Fig. 5C). Notably, partitioning of epidermal clusters by experimental conditions revealed an unidentified keratinocyte population found solely when EV-deficient ticks fed on FVB-Jax mice (Fig. 3D-I, Supplementary Dataset 3). The presence of this distinct cluster raised the hypothesis that EVs might exert an influence on keratinocytes within the context of DETCs, given its absence in FVB-Tac mice.

Tick EVs impact a keratinocyte population with a prominent wound healing signature. The emergence of this unique keratinocyte population responding to si*V33* tick feeding prompted us to further investigate their role by subjecting these cells to a subsequent round of clustering. This examination revealed keratinocyte populations at various differentiated states and highlighted the presence of an unidentified epidermal population (Fig. 4A, Supplementary Dataset 6). Next, we relied on pseudotime to align keratinocytes along an inferred developmental trajectory based on their expression profile (Fig. 4B). Gene expression signatures mirrored the sequence of differentiation, starting with markers associated with undifferentiated basal states to terminally differentiated keratinocytes (Supplementary Fig. 6). We identified a unique keratinocyte population present along the pseudotime axis of the condition where EV deficient ticks fed on FVB-Jax mice (FVB-Jax si*V33*), setting it apart from the other treatments (Fig. 4B).

The heterogeneity of keratinocytes is crucial for various functions, both during homeostasis and in response to external stimuli (Rice & Rompolas, 2020). Their transcriptional program has been recently explored to elucidate how different populations aid in the coordination of broader cellular circuits (Joost et al., 2020; Joost et al., 2018; Joost et al., 2016). Thus, we unraveled the transcriptional program employed by this unique keratinocyte population where EV deficient ticks fed on FVB-Jax mice. We computationally separated keratinocyte

populations according to their respective experimental conditions (Supplementary Fig. 7). Then, we assessed marker genes in the keratinocyte population where EV deficient ticks fed on FVB-Jax mice, which revealed elevated expression of *Col1a1*, *Col1a2*, and *Col3a1* (Fig. 4C). Evaluation of the marker gene *Col1a1* across pseudotime further underscored the distinct transcriptional program of this unique keratinocyte subcluster (Fig 4D). Altogether, these results suggested an increase in the collagen production by this keratinocyte population in response to feeding of EV-deficient ticks.

Pathway enrichment analysis of all significant marker genes in the unidentified keratinocyte population revealed an overrepresentation of genes associated with the wound healing circuitry, including growth factor, collagen, fibronectin and heparin binding, and phosphoinositide 3-kinase (PI3K) activity (Fig. 4E, Supplementary Dataset 7). These molecules have been implicated in keratinocyte function during wound healing, primarily by enhancing keratinocyte proliferation and migration to support re-epithelialization and tissue repair (Bártolo et al., 2022; Matsuura-Hachiya et al., 2018; Misiura et al., 2020). Our findings suggested that a unique keratinocyte population with a prominent wound healing signature was selectively responding to EV-deficient ticks during hematophagy. To make a comparison between EV-deficient and EV-sufficient ticks in the murine skin, we subjected keratinocytes to a differential expression analysis and assessed enriched pathways through ingenuity pathway analysis (IPA). Notably, we observed a wound healing signature in the skin of DETC-sufficient mice fed with EV-deficient ticks, which was not detected in animals deficient for DETCs (Fig. 4F).

Further inspection of differentially expressed genes annotated for wound healing revealed a decrease in transcript levels for *Fos* and *Jun* and an increase of expression for *Col1a1* and *Col1a2* (Fig. 4G, Supplementary Dataset 8). *Fos* and *Jun* are subunits of AP-1, which is important for epithelial proliferation and differentiation (Angel et al., 2001; Li et al., 2003). Conversely, collagens have various roles during all stages of wound healing, aiding in the regulation of the wound healing response, reinforcing barrier integrity and facilitating the

stratification of epidermal layers (Matsuura-Hachiya et al., 2018). Collectively, tick EVs impaired wound healing through specific molecular pathways in keratinocytes.

Tick EVs interfere with keratinocyte proliferation. To understand how tick EVs influenced wound healing in keratinocytes, we then evaluated molecular networks altered in the epidermis of DETC-sufficient and DETC-deficient mice. We performed a similar analysis in naive animals to exclude confounding effects originated from genetic differences occurring between these two strains. Four pathways were identified: eukaryotic Initiation Factor 2 (EIF2), natural killer (NK) cell, sirtuin signaling, and the unfolded protein response (UPR) (Fig. 5A, Supplementary Dataset 9). The results obtained concerning NK cell, sirtuin signaling, and the UPR pathways were likely due to the *skint1* deficiency in FVB-Tac mice. However, the EIF2 cascade was dependent on tick EVs because the computational prediction occurred regardless of the mouse genetic background (yellow highlight, Fig. 5A).

A granular view of the EIF2 signaling pathway displayed PI3K as part of the biological circuit targeted by tick EVs (Fig. 5B, Supplementary Dataset 10). The PI3K/Akt pathway is important for skin development and wound healing, two processes dependent on keratinocyte proliferation and differentiation (Calautti et al., 2005). Upon injury, keratinocytes adjacent to the wound are quiescent, opting for a migratory phenotype that allows for the initiation of re-epithelialization (Dekoninck & Blanpain, 2019). Conversely, keratinocytes farther from the wound edge undergo a proliferative burst, allowing for the closure of the gap generated by migratory keratinocytes (Aragona et al., 2017). Given that the PI3K/Akt/mTOR pathway has been observed in the proliferative zone and correlates with accelerated wound closure, we reasoned that tick EVs interfered with keratinocyte proliferation. To evaluate this hypothesis, we used the protein Ki-67 and flow cytometry as a readout for proliferative keratinocytes (Supplementary Fig. 8). We observed a significant reduction in keratinocyte proliferation when EV-sufficient ticks fed on wildtype mice (Fig. 5C). However, the effect of keratinocyte

proliferation was not observed in the absence of tick EVs (Fig. 5C). As noted above, the impact of tick feeding on keratinocyte proliferation was fully dependent on DETCs. In the absence of DETCs, the observed phenotype for keratinocyte proliferation in EV-sufficient ticks did not occur (Fig. 5C). Taken together, our reductionist approach orthogonally validated our scRNA-seq results, demonstrating that tick EVs decrease keratinocyte proliferation, which is a key step in wound healing.

The genetic constitution of a mouse may lead to substantial alterations in phenotypic traits (Tanner & Lorenz, 2022; Woodworth et al., 2004). We therefore investigated the ability of *I. scapularis* to interfere with keratinocyte homeostasis in C57BL/6 mice, a more commonly used strain. We ascertained the keratinocyte PI3K status by flow cytometry due to its ability to assess protein expression on limited cell counts. Variation in the total PI3K comparing keratinocyte populations among treatments was not observed (Fig. 5D). However, a decrease in phospho-PI3K-positive keratinocytes was recorded when ticks deficient in EVs fed on C57BL/6 mice (Fig. 5E). Additionally, the bite of *I. scapularis* ticks reduced levels of the growth factor KGF and increased levels of TGF-β in the skin, compared to the EV-deficient treatment (Fig. 5F-G). These findings correlated to a significant decrease in the frequency of $EpCAM^{+}$ keratinocytes expressing the negative regulator of TGF-β signaling, Smad7, in skin infested with *scV33* ticks compared to *siV33* ticks. (Fig. 5H; Supplementary Fig. 8). Next, we observed a significant decline in the frequency of $EpCAM^{+}$ $Ki67^{+}$ keratinocytes when EV-sufficient ticks fed on C57BL/6 mice (Fig. 5I). Remarkably, the ability of ticks to impair keratinocyte proliferation was observed in a density-dependent manner. As the number of ticks feeding on C57BL/6 mice increased, the capacity of keratinocytes to proliferate decreased (Fig. 5J). This observation was not recorded in mice infested with ticks deficient for EVs (Fig. 5K). In summary, we uncovered that tick EVs: (*i*) impacted keratinocyte proliferation; (*ii*) suppressed KGF and PI3K activity; and (*iii*) enhanced TGF- β levels, thereby, maintaining successful arthropod hematophagy.

Discussion

Ticks are ancient hematophagous arthropods that co-evolved with their hosts for millions of years (Sonenshine & Roe, 2014). Currently, we have a limited understanding of the mechanisms employed by these ectoparasites to feed on a mammal and enable pathogen transmission. Previously, we implicated *Ixodes scapularis* EVs in promoting fitness and generating distinct outcomes of pathogen transmission. This was accomplished through the SNARE protein Vamp33 and DETCs (Oliva Chávez et al., 2021). Here, we connect the mammalian wound healing circuitry as a target of tick-mediated host immunomodulation via salivary EVs. Our work connects *in vivo* proliferation of keratinocytes as a tick EV regulatory process during hematophagy.

We established the importance of EVs as a conserved strategy for arthropod fitness in three medically relevant tick species: *I. scapularis*, *A. americanum*, and *D. variabilis*. We demonstrated that *I. scapularis* EVs led to a decrease in DETCs at the bite site; yet DETCs present in the skin epidermis displayed upregulated co-stimulatory molecules. During skin injury, DETCs are activated whereby recognition of self-antigens on damaged or stressed keratinocytes allows for the orchestration of a host response (Jameson et al., 2004). Reduction of DETCs at the tick-skin interface may not be a result of cellular migration. DETC migration is facilitated by the conversion of a dendrite to a rounded morphology, which is partially regulated by CD100 signaling (Jameson et al., 2002; Witherden et al., 2012). To capture morphological changes, we employed intravital microscopy in an EV-injected triple-reporter mouse model (Park et al., 2021). Our results suggested that DETCs may not migrate during tick feeding due to the lack of cell rounding and CD100 upregulation. Importantly, DETCs regulate epidermal homeostasis and coordinate a wound healing response together with epidermal cells (Jameson et al., 2002). Collectively, our data suggest that tick EVs alter epidermal immune surveillance by restricting DETC presence and altering cell surface receptor expression, ultimately disrupting epidermal function and promoting hematophagy.

By employing a scRNA-seq approach in a mouse model naturally devoid of DETCs, we characterized the epidermal response to tick infestation. We revealed a unique keratinocyte population when EV-deficient ticks fed on DETC-sufficient mice. The absence of this unique cell population when EV-deficient ticks fed on DETC-deficient mice suggested that EVs may alter keratinocyte function within the context of intraepithelial γδ T cells. Sub clustering and pseudotime analysis of keratinocytes further emphasized the distinct nature of this unique population. Remarkably, this subcluster exhibited an overrepresentation of pathways associated with the wound healing circuitry, including growth factor, collagen and fibronectin binding, and cell proliferation. Moreover, specific biological signatures were associated with down regulation of AP-1 and upregulation of PI3K transcripts in EV-deficient tick fed on DETC-sufficient mice. These molecular circuits have been linked to epithelial proliferation and maintenance of barrier integrity in the skin epidermis (Angel et al., 2001; Jochum et al., 2001; Li et al., 2003; Matsuura-Hachiya et al., 2018).

Consistent with our systems level approach, EV-sufficient ticks fed on DETC-sufficient mice led to a decrease in keratinocyte proliferation. This observation was dependent on the role of DETCs as DETC-deficient mice did not exhibit a decrease in $Ki67^{+}$ keratinocytes. Wound healing is marked by keratinocyte proliferation and migration to restore barrier function of the epidermis (Dekoninck & Blanpain, 2019). For instance, proliferation was deemed as a necessary step for proper wound closure at the leading edge in the murine tail (Aragona et al., 2017). Conversely, proliferation was judged dispensable for wound closure in the murine ear (Park et al., 2017). Our work was done using the natural site of tick infestation in mammals, the skin of the dorsal neck. Whether proliferation is necessary for migration during a tick bite remains to be determined.

KGF serves as a strong mitogenic factor for both mouse and human keratinocytes, and its overexpression can lead to a hyperproliferative state associated with skin disorders (Ni & Lai, 2020). Upon damage of the skin, activated DETCs secrete KGF to promote wound repair

(Jameson et al., 2002). We observed that tick feeding on mice led to decreased KGF levels compared to the EV-deficient treatment. We also postulated that tick EVs interfered with other components of the wound healing biological program, including PI3K and TGF-β. We observed decreased levels of phosphorylated PI3K during EV-sufficient tick feeding on C57BL/6 mice, mirroring the findings from the scRNA-seq studies. Furthermore, we observed an increase in TGF-β release during tick feeding, which correlated to lower Smad7 levels compared to EV-deficient feeding at the bite site. Increased levels of TGF-β in the epidermis have been associated with the inhibition keratinocyte proliferation (Sellheyer et al., 1993). Moreover, TGF-β transduction is mediated by SMAD proteins, with Smad7 acting as a negative regulator of the TGF-β signaling network (Schmierer & Hill, 2007). Thus, we suggest that the observed reduction of DETCs during tick feeding may obstruct the necessary levels of KGF and TGF-β in the epidermis during wounding.

Extracts from tick salivary glands have shown their capability to impede cellular growth *in vitro* (Hajnicka et al., 2011). Accordingly, we demonstrated *in vivo* that tick EVs led to a significant reduction in the frequency of $Ki67^{+}$ keratinocytes. Strikingly, the ability of ticks to impair epithelial cell proliferation was observed in a quantitative-dependent manner. An increase in the number of ticks fed simultaneously at a given skin site, resulted in a decrease of proliferative keratinocytes. In sum, this study unveiled the immunomodulatory effects of tick EVs in the epidermal layer, deviating from the established viewpoint that arthropod saliva mainly influences dermal responses.

Materials and Methods

Reagents and resources

All primers, reagents, resources, and software used in this study, together with their manufacturer's information and catalog numbers are listed in Supplementary Tables 1 and 3.

Ticks

I. scapularis nymphs were obtained from two independent sources: (1) Dr. Ulrike Munderloh and Dr. Jonathan Oliver at the University of Minnesota; and the (2) tick rearing facility at Oklahoma State University. *A. americanum* and *D. variabilis* nymphs were obtained from the tick rearing facility at Oklahoma State University. Partially engorged *I. scapularis* adult ticks were obtained from Dr. Albert Mulenga and Dr. Adela Oliva Chavez at Texas A&M University. Upon arrival, ticks were maintained in a Percival I-30BLL incubator at 23°C with 85% relative humidity and a 12/10-hours light/dark photoperiod regimen.

Mice

Experiments were performed on C57BL/6, FVB/N Jax, and FVB/N Tac mice. Breeding pairs were purchased from the Jackson Laboratory except FVB/N Tac mice, which were purchased from Taconic Biosciences. All mouse strains were bred at the University of Maryland School of Medicine, unless otherwise indicated. Male mice (7–9 weeks) were used for all experiments. All mouse experiments were approved by the Institutional Biosafety (IBC-00002247) and Animal Care and Use (IACUC numbers 0119012 and 1121014) committees at the University of Maryland School of Medicine and complied with the National Institutes of Health (NIH) guidelines (Office of Laboratory Animal Welfare [OLAW] assurance number A3200-01). *huLangerin-CreER;Rosa-stop-tdTomato;CX3CR1-GFP$^{+/-}$;K14-H2B-Cerulean* mice used for intravital microscopy imaging were housed at Michigan State University as described elsewhere (Park et al., 2021) (IACUC number PROTO202300065). To activate DETCs, Cytochalasin D

(Sigma-Aldrich, C8273) was delivered topically as previously described (Park et al., 2021). Briefly, Cytochalasin D was dissolved in a 25 mg/ml stock solution in dimethyl sulfoxide (DMSO), and later, the stock solution was diluted 100 times in 100% petroleum jelly (Vaseline; final concentration is 250 µg/ml). One hundred micrograms of the mixture of Cytochalasin D and the petroleum jelly were spread evenly on the skin once every 24 hours for 2 days. A mixture of 100% DMSO in petroleum jelly (1:100) was used as a vehicle control.

RNA interference

siRNAs and scRNAs for *vamp33* were designed as previously described (Oliva Chávez et al., 2021). Both siRNAs and scRNAs were synthesized according to the Silencer® SiRNA construction kit (Thermo Fisher Scientific). Primers are described in Supplementary Table 1. Unfed nymphs were microinjected with 60-80 ng of siRNA or scRNA using a Nanoject III (Drummond Scientific Company). Ticks recovered overnight at 23°C with saturated humidity before being placed on respective mice.

EV-depleted media

L15C300 medium was supplemented with 5% FBS (Millipore-Sigma), 5% tryptose phosphate broth (TPB) (BD), 0.1% lipoprotein concentrate (LPC) (MP Biomedicals), 0.25% sodium bicarbonate (Millipore-Sigma), and 25 mM HEPES (Millipore-Sigma). Media was cleared from EVs by ultracentrifugation at 100,000×g for 18 h at 4 °C in a LE-80 ultracentrifuge (Beckman Coulter) with a 60Ti rotor. EV-free media was then passed through a 0.22-µm Millipore Express® PLUS (Millipore-Sigma). The absence of EVs was confirmed by determining the particle size distribution with the NanoSight NS300 (Malvern Panalytical) for nanoparticle tracking analysis (NTA).

459 **Tick salivary gland culture**

460 Salivary gland EVs were purified from *ex vivo* cultures that originated from partially
461 engorged adult female ticks. Adult *I. scapularis* females were fed on New Zealand white rabbits
462 for 5–6 days at either Dr. Albert Mulenga or Dr. Adela Oliva Chavez laboratories at Texas A&M
463 University, as previously described (Oliva Chávez et al., 2021). Then, ticks were shipped to the
464 University of Maryland School of Medicine. Partially-fed adult female ticks (90-120) were
465 dissected 1–2 days post-removal. Briefly, midguts, Malpighian tubes, and other organs were
466 removed. PBS was added to samples to avoid desiccation. Salivary glands were dissected and
467 cultured in 24-well cell culture plates (Corning). 10 salivary glands from adult ticks were placed
468 in each well, containing 500 µl of L15C300 EV-free medium supplemented with 1x
469 penicillin/streptomycin (Corning) and 1x Amphotericin B (Gibco). Salivary glands were incubated
470 for 24 h at 34 °C to allow EV secretion.
471
472 **EV purification**
473 Medium collected from salivary gland cultures were cleared of any live cells by
474 centrifugation at 300 × g for 10 minutes at 4 °C. Dead cells were removed by a second
475 centrifugation at 2,000 × g for 10 minutes at 4 °C. The supernatant was collected, and apoptotic
476 bodies were removed by a third centrifugation at 10,000 × g for 30 minutes at 10°C. The
477 supernatant was filtered through a 0.22-µm Millipore syringe filter (Millipore-Sigma) to reduce
478 the number of EVs >200 nm in size. EVs were pelleted by ultracentrifugation (100,000 × g) for
479 18 hours at 4 °C. Supernatant was discarded and EVs were resuspended in PBS. EV
480 concentration and sizes were determined using the NanoSight 300 machine (Malvern
481 Panalytical) with the software versions 2.0 or 3.0. The mean of the size generated in the reports
482 was used to calculate the average size of the EVs in each sample. The concentration of
483 proteins in tick EVs was determined using the BCA assay (Thermo Scientific), following the
484 manufacturer's procedure.

485

486 **Mouse capsule placement**

487 Capsules made from the upper portion of a snap or screw top tube were adhered to the
488 dorsal neck of each mouse to contain the ticks in one area. This technique is referred to as the
489 capsule-feeding method and was adapted from a previous study (Schoeler et al., 1999). Briefly,
490 capsule adhesive solution was made from 3 parts gum rosin (Sigma-Aldrich) and 1 part
491 beeswax (FisherScience). Mice were anesthetized using isoflurane and shaved between the
492 shoulder blades to the top of the cranium. Capsules were applied with the warmed adhesive
493 and allowed to dry up for 24 hours prior to tick placement. Capsules were sealed with either a
494 glued piece of mesh or a screw top after tick placement. Naïve groups consisted of capsule
495 placement without ticks.

496

497 **Tick feeding experiments**

498 Microinjected ticks were placed on mice using either the free-feeding or capsule-feeding
499 method and allowed to feed for 3 days. On day 3, ticks were collected, weighed, and either
500 placed in a humidified chamber for survival analysis or frozen at −80°C for RNA purification. To
501 purify the mRNA, ticks were flash-frozen in liquid nitrogen and crushed with small plastic
502 pestles. TRIzol® reagent (200 µl) was added to the crushed tick and RNA was purified using the
503 PureLink™ RNA mini kit. cDNA was synthesized from 50 to 200 ηg (5–10 µl) of RNA using the
504 Verso cDNA synthesis kit (Thermo scientific).

505

506 **Quantitative reverse transcription polymerase chain reaction (qRT-PCR)**

507 qRT-PCR was performed to measure gene expression. qRT-PCR was performed with
508 the CFX96 Touch Real-Time PCR Detection 233 System (Biorad). No template controls were
509 included to verify the absence of primer-dimers formation and/or contamination. Reactions on

each sample and controls were run in duplicate. Gene expression was determined by relative quantification normalized to the tick *actin*, using the primers listed in Supplementary Table 1.

Flow cytometry of skin cell populations

I. scapularis nymphs fed on C57BL/6, FVB/N Jax, or FVB/N Tac male mice. On the third day of feeding, mice were euthanized with CO_2. A 10- or 5-mm skin punch biopsy was taken while ticks were still attached. Skin samples from un-infested control mice were collected from matching locations. Single cell suspensions were prepared from each skin sample. Briefly, skin samples were cut into small pieces with sterile surgical scissors and placed into round-bottom tubes containing digestion buffer consisting of 90% RPMI-1640 (Quality Biological), 10% Liberase™ TL Research Grade (Roche), and 0.1% DNAse I (Millipore-Sigma). Digestions were carried out for 1 hour and 15 minutes at 37°C with constant shaking. Single cell suspensions were obtained by passing the digested tissues through a 40-µm cell strainer (Corning), homogenizing the tissue with a plunger and flushing cells with wash buffer consisting of PBS and 2 mM EDTA. Cells were centrifuged at 300 x g for 5 minutes at 4 °C, resuspended in 1 ml FACS buffer (PBS containing 1% BSA, 2 mM EDTA, and 0.05% NaN3) or FACS intracellular buffer (PBS containing 1% BSA and 0.05% NaN3). Cell suspensions were placed into a 96-well U-bottom plate and stained with respective antibody panels.

Live and dead cells were discriminated using Zombie Violet Fixable Live Dead stain (BioLegend). Cells were washed with FACS buffer. Cells were then blocked with anti-FcR (CD16-CD32) (BioLegend 156603), and subsequently stained with the respective antibody panel for 15 minutes at 4°C and washed with FACS buffer. Whenever appropriate, anti-rat IgM was added to the cells, incubated for 15 minutes at 4°C, and washed twice with the FACS buffer. Finally, cells were resuspended in 4% paraformaldehyde. For intracellular staining, cells were further processed following the instructions for the BioLegend's FOXP3 Fix/Perm Buffer Set kit. Cells were measured with a LSRII flow cytometer (BD) at the Flow & Mass Cytometry

Facility at the University of Maryland School of Medicine. Analysis was performed using the FlowJo software.

DETC populations in the murine skin were labeled with APC anti-CD45 (BioLegend 103111) or PE/Cyanine7 anti-CD45 (BioLegend 103114), FITC anti-CD3 (BioLegend 100203), BV60 anti-Vγ5 (BD 743241), APC anti-Thy1.2 (BioLegend 105312), and/or monoclonal antibody 17D1 (kindly provided by Dr. Adrian Hayday, King's College London, and Dr. Robert Tigelaar, Yale University), and PE mouse anti-rat IgM (BD 553888). DETC costimulatory markers were measured with PE anti-JAML (BioLegend 128503), BV711 anti-CD100 (BD 745492), PE/Cyanine5 anti-CD44 (BioLegend 103010), APC/Cyanine7 anti-CD25 (BioLegend 102026), PerCP/Cyanine5.5 anti-CD69 (BioLegend 104522), and APC anti-CD314 (BioLegend 130212). Keratinocyte populations in the murine skin were labeled with BV711 anti-CD324 (BioLegend 118233), PE anti-CD200 (BioLegend 123807), PE/Cyanine5 anti-CD34 (BioLegend 119312), BV605 Sca1 (BioLegend 108133), and/or PE anti-CD49f (BioLegend 313612). Keratinocyte proliferation was labeled with the Alexa Fluor 700 anti-Ki-67 (BioLegend 652420). Smad7 was labeled with the anti-MADH7/SMAD7 polyclonal antibody (Abcam ab216428) and Alexa Fluor 405 goat anti-Rabbit IgG secondary antibody (Thermo Fischer Scientific A-31556).

Enzyme-linked immunosorbent assay

To determine levels of KGF, 5 mm skin biopsies were placed in 200µL of RPMI media tissue bath for one hour shaking at 32°C (150 revolutions per minute). KGF levels in tissue bath supernatant were determined using the R&D Systems KGF/FGF-7 Quantikine ELISA kit according to manufacturer instructions. To determine levels of TGF-β, 5mm skin biopsies were homogenized in lysis buffer containing 1X RIPA buffer (catalogue number 20-188, Millipore) with 1X protease-phosphatase inhibitor cocktail (catalogue number 78420, Thermo Scientific). TGF-β levels in tissue supernatant were determined using the R&D Systems TGF-β 1 Quantikine

ELISA kit according to manufacturer instructions. Total protein in samples was determined using the Pierce BCA Protein Assay Kit (catalogue number 23227 Thermo Scientific). Sample concentration of KGF/TGF-β were normalized to the total protein in a sample.

Intravital microscopy

Epidermal intravital imaging studies were done in collaboration with Dr. Sangbum Park at Michigan State University. All *in vivo* imaging and analysis were performed, as described previously (Park et al., 2021). Simultaneous visualization of Langerhans cells, DETCs and epithelial cells was achieved by utilizing the *huLangerin-CreER;Rosa-stop-tdTomato;CX3CR1-GFP*$^{+/-}$*;K14-H2B-Cerulean* mice.

Epidermal single-cell isolation, scRNA-seq library preparation and sequencing

I. scapularis nymphs were microinjected with *vamp33* si or *vamp33* sc and fed on FVB/N Jax or FVB/N Tac mice. On the third day of feeding, mice were euthanized with CO_2. Partially fed ticks were removed and the sites where ticks bit were shaved followed by an application of a light layer of Nair depilatory lotion. A total of three 5-mm skin punch biopsies were obtained from the dorsal neck for each mouse. 5-mm skin punch biopsies were obtained from the same physiological site of naïve mice. Skin samples were incubated in dispase solution (4 U/mL dispase, 5mM MgCl2, and 0.4mM CaCl2 in PBS) for 2.5 hours at 37°C with constant shaking/stirring. Epidermal sheets were separated from the dermal layer using forceps. Epidermal sheets were then incubated in a digestion solution (2.5mg/mL collagenase D and 0.2mg/mL DNase in RPMI Medium) for 1 hour at 37°C with constant shaking/stirring.

Cells were resuspended using a wide-bore pipette tip and three samples per treatment per mouse were combined. Samples were passed through a 40 μM cell strainer and washed with RPMI +10% FBS. Cells were counted using the Countess II FL Automated Cell Counter, stained with 5 μl of 7-AAD per million cells, and incubated in the dark for 10 minutes at 4°C.

Samples were then sorted at the CIBR Flow Cytometry Core Facility at the University of Maryland School of Medicine. Cells were sorted into a PBS in the absence of calcium and magnesium + 10% FBS collection buffer. They were then transported on ice to the Institute of Genome Sciences at the University of Maryland School of Medicine for library preparation and sequencing. Single cell libraries were generated with the 3' NextGEM v3.1 kit targeting 3800-5000 cells. Libraries were sequenced with a NovaSeq 6000, S2 flowcell targeting 375M read pairs per sample.

Bioinformatics

All scRNA-seq reads were processed and mapped to the mouse mm10 reference genome using 10X Genomics' Cell Ranger software. Approximately 20,640 total cells were profiled with 88,027 mean reads per cell across all conditions. A count matrix (gene-by-cell) generated by cell ranger count for each library was then aggregated into a single count matrix. Expression matrices were generated using the Bioconductor packages scater (v1.22.0) (Lun, McCarthy, et al., 2016) and scran (v1.22.1) (Lun, Bach, et al., 2016). Cells with less than 2,500 or greater than 60,000 UMIs were removed after calculating cell metrics using scater (v1.22.0). DoubletFinder (v2.0.1) (McGinnis et al., 2019) was applied removing 1,364 cells, which yielded a total of 10,715 cells. The remaining transcriptomes were normalized by first calculating size factors via the scran functions quickCluster and computeSumFactors. Then, we computed normalized counts for each cell with logNormCounts function in scran (v1.22.1).

For downstream analysis, highly variable genes were selected using getTopHVGs before performing the Principal Component Analysis (PCA) and the tSNE projection. Clustering was conducted using kmeans function based on the calculated tSNE. Differential gene expression between clusters was calculated using find Markers function. Only identified epidermal cells of interest (Keratinocytes, T cells, and APCs) were further analyzed, resulting in a total of 5,172 cells with a median UMI count of 13,910 per cell. For pseudotime analysis, the Bioconductor

matrix was imported into slingshot (v2.2.1) (Street et al., 2018). To compare the T cell receptor delta variable 4 (*Trdv4*) expression, normalized counts were used for visualization by the violin plot. The permutation test was applied to calculate the significance of the difference in the mean expression between two groups. A list of differentially expressed keratinocyte genes between treatments was generated by MAST (v1.24.0) (Finak et al., 2015) with significance testing under the Hurdle model for downstream analysis by the IPA.

Gene set enrichment analysis

Gene set enrichment analysis was performed using DAVID, version 2021. Default DAVID parameters were employed and included the following categories for the enrichment analysis: GOTERM_BP_DIRECT, GOTERM_CC_DIRECT and GOTERM_MF_DIRECT (from Gene_Ontology), KEGG_PATHWAY (from Pathways) and INTERPRO (from Protein_Domains). *p* value and FDR< 0.05 were set as a threshold.

Ingenuity pathway analysis

Differentially expressed keratinocyte genes from the following samples were analyzed in the IPA as independent datasets: 1) FVB-Tac Naïve versus FVB-Jax Naïve 2) FVB-Jax si*V33* versus FVB-Jax sc*V33* and 3) FVB-Tac si*V33* versus FVB-Tac sc*V33*. Genes were considered differentially expressed if the *p* value and FDR were < 0.05. Dataset input criteria for the IPA included expression, *p* value, log ratio, FDR, and Ensemble ID codes. All datasets were examined for canonical pathway and upstream regulator analysis. FVB-Tac Naïve versus FVB-Jax Naïve dataset had 591 IDs, including 589 mapped and 2 unmapped IDs. FVB-Jax si*V33* versus FVB-Jax sc*V33* dataset had 1207 IDs, including 1204 mapped and 3 unmapped IDs. FVB-Tac si*V33* versus FVB-Tac sc*V33* had 732 IDs, including 728 mapped and 4 unmapped IDs. The IPA proprietary algorithm segments the network map between molecules into multiple networks and assigns scores for each network as described previously (Calvano et al., 2005).

For the canonical pathway analysis, −log (P-value) >2 was taken as threshold and for the upstream regulator analysis, the *p* value of overlap <0.05 was set as the threshold. A positive *Z*-score was defined as the predicted activation, and a negative *Z*-score was defined as the predicted inhibition.

Statistical analysis

Statistical significance was assessed as follows: percent tick attachment was calculated by the Fisher's exact test, tick weight by the *t* test or the Mann Whitney test, and survival curve by the Log-rank (Mantel-Cox) test. One-way ANOVA followed by Tukey's *post hoc* test for multiple comparisons was also used. Kruskal-Wallis ANOVA was implemented if the dataset failed normality of residuals or displayed heterogeneity of variance. We used GraphPad PRISM® (version 9.1.0) for all statistical analyses. Outliers were detected by a GraphPad Quickcals program (https://www.graphpad.com/quickcalcs/Grubbs1.cfm). *p* values of < 0.05 were considered statistically significant.

Acknowledgements

We acknowledge members of the Pedra laboratory for providing insightful discussions. We thank the rearing facility at Oklahoma State University for providing *I. scapularis, A. americanum,* and *D. variabilis* ticks; Xiaoxuan Fan, Bryan Hahn, Regina Harley, and Sean McGill (University of Maryland School of Medicine) for flow cytometry and sorting assistance; Adrian Hayday (King's College London) and Robert Tigelaar (Yale University) for the monoclonal antibody 17D1; the Maryland Genomics Core at the Institute for Genome Sciences, University of Maryland School of Medicine for the services provided in next generation sequencing; the University of Maryland Greenebaum Comprehensive Cancer Center Flow Cytometry Shared Service core facility and the Flow & Mass Cytometry Facility at the University of Maryland School of Medicine for flow cytometry services; Cristiana Cairo, Nevil Singh, Nicholas Carbonetti (University of Maryland School of Medicine) and Jere McBride (University of Texas Medical Branch) for insightful advice. This work was supported by grants from the NIH to F31AI152215 (AJO), F31AI167471 (LRB), R01AI134696 (JHFP), R01AI116523 (JHFP), P01AI138949 (JHFP), T32AI162579 (HJL-Y), R01AR083086 (SP), the United States Department of Agriculture, National Institute of Food and Agriculture (USDA-NIFA) Hatch-Multistate Project to TEX0-1-7714 (AOC), and the Knipling-Bushland-Swahrf fellowship from the Department of Entomology at Texas A&M University (BL-G). The content is solely the responsibility of the authors and does not represent the official views of the NIH, the Department of Health and Human Services, the USDA-NIFA or the United States government.

Data and Code Availability

All scRNA sequences are deposited into the NCBI Sequence Read Archive under the BioProject accession PRJNA905677. R codes for scRNA sequencing datasets were adapted from https://bioconductor.org/books/3.16/OSCA/ and specified R package vignettes. Tokens can be made available upon request.

Resource Availability

Further information and request for resources and reagents should be directed to and will be honored by the corresponding author: Joao HF Pedra (jpedra@som.umaryland.edu)

Author contributions

LM and JHFP designed the study. LM and LMV performed the experiments. HNB, HJL-Y and AR performed computational analysis. AJO, LRB, CRF, ADS-S, DMR, MTM, SS, NS, and FECP aided with experimentation. EBC, T-TN, BL-G, ASOC, AM, UGM and JDO provided ticks. LM, LV and JHFP wrote the manuscript. LRB created illustrations. JMJ, SP, and DS supervised experiments and/or provided resources and guidance. JHFP supervised the study. All authors analyzed the data, provided intellectual input into the study, and contributed to editing of the manuscript.

Figure Legends

Figure 1: Tick EVs affect hematophagy and survival. (A) Graphical illustration of experimental design. **(B-M)** *Vamp33* siRNA (*siV33*) (red) or *vamp33* scramble control (*scV33*) (blue) microinjected nymphs were placed on C57BL/6 mice and allowed to feed for 3 days. On day 3, ticks were harvested and assessed for fitness measurements. Efficiency of *Vamp33* silencing and tick attachment, weight, and survival curves for **(B-E)** *I. scapularis,* **(F-I)** *A. americanum* and **(J-M)** *D. variabilis.* Graphs represent at least three independent experiments combined. Statistical significance shown as **p*<0.05, ***p*<0.01, ns = not significant was assessed by *t* test **(B, F, J)**; Fisher's exact test **(C, G, K)**; Mann Whitney test **(D, H, L)**; and Log-rank (Mantel-Cox) test **(E, I, M)**.

Figure 2: Tick EVs alter epidermal immune surveillance. (A) Schematic representation of the DETC-keratinocyte crosstalk at the skin epidermis. **(B-F, H)** *I. scapularis scV33* (blue) or *siV33* (red) ticks were placed on C57BL/6 mice and allowed to feed for 3 days. On day 3, biopsies were taken from the skin at the bite site and compared to the naïve treatment (gray). **(B)** DETC (Vγ5), **(C)** JAML, **(D)** NKG2D, **(E)** CD69, **(F)** CD25, and **(H)** CD100 cells were assessed by flow cytometry. Graphs represent 1 of 3 independent experiments. **(G)** Epidermis containing Langerhans cells (red), DETCs (green), and keratinocytes (white) imaged on day 3 after injection with phosphate buffered saline (PBS - mock) or EV ($4x10^7$ particles) into the mouse ear. Cytochalasin D (100 µg) was applied topically on the mouse ear every 24 hours for 2 days to induce DETC rounding as a positive control. Langerhans cells, DETCs and epithelial cells were simultaneously visualized in the *huLangerin-CreER; Rosa-stop-tdTomato; CX3CR1-GFP*$^{+/-}$*; K14-H2B-Cerulean* mouse strain. Cre expression was induced with an intraperitoneal injection of tamoxifen (2 mg). Images from one out of three independent experiments. Statistical significance shown as **p*<0.05, ns = not significant. Data are presented as a mean with

719 standard deviation. Significance was measured by One-way ANOVA followed by Tukey's *post*
720 *hoc* test.
721
722 **Figure 3: Epidermally-enriched scRNA-seq of the tick bite site. (A)** Overview of the
723 experimental design. *ScV33* and *siV33 I. scapularis* nymphs were placed on FVB-Jackson
724 (FVB-Jax) or FVB-Taconic (FVB-Tac) mice and fed for 3 days. Skin biopsies at the bite site were
725 digested with dispase and collagenase for epidermal cell isolation. Cells were sorted and
726 prepared for scRNA-seq. **(B)** Composite tSNE plot of keratinocyte, T cell and antigen presenting
727 cells in FVB-Jax and FVB-Tac mice in the presence or absence of *I. scapularis* nymphs
728 microinjected with *scV33* or *siV33*. tSNE plot represents 5,172 total cells following filtration as
729 described in the materials and methods. **(C)** Heatmap depicting expression of the top 5 marker
730 genes present in clusters from the epidermally enriched tSNE plot clusters (as shown in **B**). **(D-**
731 **I)** Individual tSNE plots separated by mouse strain (FVB-Jax or FVB-Tac) in the presence or
732 absence of *I. scapularis* nymphs microinjected with *scV33* or *siV33*.
733
734 **Figure 4: Impact of tick EVs on wound healing circuitry. (A)** Composite tSNE plot of
735 keratinocytes in FVB-Jax and FVB-Tac mice in the presence or absence of *I. scapularis* nymphs
736 microinjected with *scV33* or *siV33*. **(B)** Cells colored by clusters originated from the keratinocyte
737 tSNE plot (as shown in **A**) ordered across pseudotime (x-axis) for naïve, *scV33*-, and *siV33*-tick
738 bites of FVB-Jax and FVB-Tac mice. **(C)** Dot plot of the top 5 marker genes present in the
739 keratinocyte clusters (as shown in **A**). Average gene expression is demarked by the intensity of
740 color. Percent of gene expression within individual clusters is represented by the dot diameter.
741 **(D)** Expression of *Col1a1* across treatments ordered across pseudotime (x-axis) for naïve,
742 *scV33*-, and *siV33*-tick bites of FVB-Jax and FVB-Tac mice. **(E)** Enriched pathways in the
743 unidentified cell cluster based on functional annotation in DAVID. Fold enrichment is indicated in
744 a Log2 scale. *p value and false discovery rate (FDR)<0.05 were set as threshold. KEGG, GO

and InterPro were used as reference annotation databases. **(F)** Ingenuity pathway analysis comparing keratinocytes of skin biopsies from FVB-Jax *siV33* to FVB-Jax *scV33*. Blue denotes pathways predicted to be inhibited (negative z-score) whereas orange indicates pathways predicted to be activated (positive z-score) based on default parameters. Differential expression datasets were assessed for canonical pathway analysis. Results are shown in a -log (*p*-value) scale. **p* value and FDR< 0.05 were set as threshold. **(G)** Volcano plot of genes representing the wound healing signaling pathway in keratinocytes of FVB-Jax *siV33* compared to FVB-Jax *scV33* datasets (highlighted in yellow; **F**). Blue denotes decrease whereas red indicates increase in the coefficient (coef) of expression.

Figure 5: Tick EVs impact keratinocyte proliferation. (A) Ingenuity pathway analysis derived from *siV33* compared to the bite of *scV33* ticks on FVB-Jax or FVB-Tac mice. Canonical pathways predicted to be inhibited (blue, negative z-score) or activated (orange, positive z-score) based on differential expression profile. The solid line indicates the *p* value significance threshold of 0.05 (-log=1.3). **(B)** The signaling cascade of EIF2 (highlighted in yellow, **A**), yielding (→) or inhibitory (⊣) arrows. Orange indicates activation whereas blue shows inhibition according to the IPA prediction. Gene expression based on the scRNA-seq experiment is indicated in red (increased) or green (decreased). Gray – denotes no expression or prediction. **(C)** *ScV33* (circle) or *siV33* (square) injected *I. scapularis* nymphs were fed on FVB-Jax (white) or FVB-Tac (gray) mice for 3 days. Biopsies were taken from the skin at the bite site and assessed for $EpCAM^+$ $Ki67^+$ keratinocytes by flow cytometry. **(D-H)** *ScV33* or *siV33* ticks fed on C57BL/6 mice for 3 days. Biopsies were taken from the skin at the bite site and processed for flow cytometry analysis. **(D)** PI3K $p85^+$, and **(E)** phospho-PI3K p85/$p55^+$. **(F)** ELISA analysis of KGF levels normalized to total protein per 5 mm skin punch biopsy. **(G)** ELISA analysis of TGF-β levels normalized to total protein per 5 mm skin punch biopsy. **(H)** $EpCAM^+$ $Smad7^+$ keratinocytes assessed by flow cytometry. **(I)** $EpCAM^+$ $Ki67^+$ keratinocytes assessed by flow

771 cytometry. Graph displays proliferation changes within the *scV33* or *siV33* treatments compared
772 to the naïve skin. **(C-I)** Significance was measured by One-way ANOVA followed by Tukey's
773 post hoc test. **(J-K)** Flow cytometry histogram plots of $EpCAM^{+}$ $Ki67^{+}$ keratinocytes. **(J)** *scV33*
774 or **(K)** *siV33* treatments displayed according to the number of ticks bitten per biopsy. X-axis
775 shows fluorescence intensity, and the Y-axis indicates the count of events in the fluorescence
776 channel. All experiments have statistical significance shown as ***p<0.001, **p<0.01, *p<0.05,
777 ns = not significant. Data are presented as a mean with standard deviation.

Supplementary Figure Legends

Supplementary Figure 1: DETC flow cytometry gating strategy. 5 mm skin punch biopsies were obtained from the bite of ticks and compared to the naïve skin followed by flow cytometry analysis. Representative flow cytometry plots were gated for **(A)** DETCs ($Vγ5^+$) and **(B)** DETC co-receptors ($JAML^+$, $NKG2D^+$, $CD25^+$, $CD69^+$, $CD100^+$ or $CD44^+$).

Supplementary Figure 2: ScRNA-seq data filtration. Composite datasets of FVB-Jax and FVB-Tac samples included 20,640 cells **(A)** before filtration by scran (R package). **(B)** tSNE plot of fixed threshold filtration, set to 2500-60,000 UMIs. **(C)** Doublet finder (R package) of dataset. tSNE was colored by the doublet score. **(D)** tSNE plot after fixed threshold filtration and doublet finder analysis.

Supplementary Figure 3: Expression of keratinocyte-specific markers. (A) Graphical illustration of keratinocyte stratified layers with select marker genes. tSNE of keratinocyte clusters depicting gene expression of **(B)** *Krt14*, **(C)** *Krt5*, **(D)** *Krt1*, **(E)** *Krt10* and **(F)** *Ivl*.

Supplementary Figure 4: Expression of hair follicle-specific markers. (A) Graphical illustration of hair follicle microanatomy with select marker genes. tSNE of keratinocyte clusters depicting gene expression of **(B)** *Shh*, **(C)** *Krt75*, **(D)** *Lgr5*, **(E)** *Mgst1* and **(F)** *Krt79*.

Supplementary Figure 5: Epidermal cell type characterization. Cluster frequency of keratinocytes, antigen presenting and T cells in **(A)** FVB-Jax and **(B)** FVB-Tac mice in the presence or absence of *I. scapularis* nymphs microinjected with *scV33* or *siV33*. **(C)** Violin plot displaying the expression of the TCR-Vδ1 gene, *Trdv4*, in the epidermal T cell cluster of naïve FVB-Jax and FVB-Tac mice. Significance shown as $*p<0.05$ based on a permutation test using R statistical packages.

Supplementary Figure 6: Keratinocyte-specific markers along pseudotime trajectory. (A) *Krt14*, **(B)** *Krt1*, and **(C)** *Ivl* gene expression along pseudotime values (x axis) for naïve, *scV33*-, or *siV33*-tick bites on FVB-Jax or FVB-Tac mice. Cells colored by clusters from keratinocyte tSNE plot (as shown in Figure **4D**) ordered across the pseudotime (x-axis).

Supplementary Figure 7: Individual tSNE plots of keratinocyte clusters. Subclustering analysis of keratinocytes across samples: **(A)** FVB-Jax, **(B)** FVB-Jax *scV33*, **(C)** FVB-Jax *siV33*, **(D)** FVB-Tac, **(E)** FVB-Tac *scV33*, and **(F)** FVB-Tac *siV33*.

Supplementary Figure 8: Flow cytometry gating strategy in keratinocytes. 5 mm punch biopsies were obtained from the bite site of ticks or naïve skin and processed for flow cytometry. Representative flow cytometry plots were gated for **(A)** $EpCAM^+$ keratinocytes, **(B)** $Ki67^+$, **(C)** Anti-rabbit IgG^+ for PI3K and Smad7, and **(D)** p-$PI3K^+$ keratinocytes.

References

Allen, J. R., Khalil, H. M., & Wikel, S. K. (1979). Langerhans cells trap tick salivary gland antigens in tick-resistant guinea pigs. *J Immunol*, *122* (2), 563-565.

Angel, P., Szabowski, A., & Schorpp-Kistner, M. (2001). Function and regulation of AP-1 subunits in skin physiology and pathology. *Oncogene*, *20* (19), 2413-2423. https://doi.org/10.1038/sj.onc.1204380

Aragona, M., Dekoninck, S., Rulands, S., Lenglez, S., Mascre, G., Simons, B. D., & Blanpain, C. (2017). Defining stem cell dynamics and migration during wound healing in mouse skin epidermis. *Nat Commun*, *8*, 14684. https://doi.org/10.1038/ncomms14684

Bakshi, M., Kim, T. K., Porter, L., Mwangi, W., & Mulenga, A. (2019). *Amblyomma americanum* ticks utilizes countervailing pro and anti-inflammatory proteins to evade host defense. *PLoS Pathog*, *15* (11), e1008128. https://doi.org/10.1371/journal.ppat.1008128

Barbee, S. D., Woodward, M. J., Turchinovich, G., Mention, J. J., Lewis, J. M., Boyden, L. M., Lifton, R. P., Tigelaar, R., & Hayday, A. C. (2011). Skint-1 is a highly specific, unique selecting component for epidermal T cells. *Proc Natl Acad Sci U S A*, *108* (8), 3330-3335. https://doi.org/10.1073/pnas.1010890108

Bártolo, I., Reis, R. L., Marques, A. P., & Cerqueira, M. T. (2022). Keratinocyte growth factor-based strategies for wound re-epithelialization. *Tissue Eng Part B Rev*, *28* (3), 665-676. https://doi.org/10.1089/ten.TEB.2021.0030

Bernard, Q., Grillon, A., Lenormand, C., Ehret-Sabatier, L., & Boulanger, N. (2020). Skin interface, a key player for *Borrelia* multiplication and persistence in Lyme borreliosis. *Trends in Parasitology*, *36* (3), 304-314. https://doi.org/https://doi.org/10.1016/j.pt.2019.12.017

Boyden, L. M., Lewis, J. M., Barbee, S. D., Bas, A., Girardi, M., Hayday, A. C., Tigelaar, R. E., & Lifton, R. P. (2008). Skint1, the prototype of a newly identified immunoglobulin superfamily gene cluster, positively selects epidermal gammadelta T cells. *Nat Genet*, *40* (5), 656-662. https://doi.org/10.1038/ng.108

844 Calautti, E., Li, J., Saoncella, S., Brissette, J. L., & Goetinck, P. F. (2005). Phosphoinositide 3-
845 kinase signaling to Akt promotes keratinocyte differentiation versus death. *J Biol Chem*, *280*
846 (38), 32856-32865. https://doi.org/10.1074/jbc.M506119200
847 Calvano, S. E., Xiao, W., Richards, D. R., Felciano, R. M., Baker, H. V., Cho, R. J., Chen, R. O.,
848 Brownstein, B. H., Cobb, J. P., Tschoeke, S. K., Miller-Graziano, C., Moldawer, L. L.,
849 Mindrinos, M. N., Davis, R. W., Tompkins, R. G., Lowry, S. F., Inflamm, & host response to
850 injury large scale collab. research program. (2005). A network-based analysis of systemic
851 inflammation in humans. *Nature*, *437* (7061), 1032-1037.
852 https://doi.org/10.1038/nature03985
853 Chen, G., Wang, X., Severo, M. S., Sakhon, O. S., Sohail, M., Brown, L. J., Sircar, M., Snyder,
854 G. A., Sundberg, E. J., Ulland, T. K., Olivier, A. K., Andersen, J. F., Zhou, Y., Shi, G. P.,
855 Sutterwala, F. S., Kotsyfakis, M., & Pedra, J. H. (2014). The tick salivary protein sialostatin L2
856 inhibits caspase-1-mediated inflammation during *Anaplasma phagocytophilum* infection.
857 *Infect Immun*, *82* (6), 2553-2564. https://doi.org/10.1128/IAI.01679-14
858 Dekoninck, S., & Blanpain, C. (2019). Stem cell dynamics, migration and plasticity during wound
859 healing. *Nat Cell Biol*, *21* (1), 18-24. https://doi.org/10.1038/s41556-018-0237-6
860 Dickinson, R. G., O'Hagan, J. E., Schotz, M., Binnington, K. C., & Hegarty, M. P. (1976).
861 Prostaglandin in the saliva of the cattle tick *Boophilus microplus*. *Aust J Exp Biol Med Sci*, *54*
862 (5), 475-486. https://doi.org/10.1038/icb.1976.48
863 Eisen, L. (2022). Tick species infesting humans in the United States. *Ticks and tick-borne*
864 *diseases*, *13* (6), 102025. https://doi.org/https://doi.org/10.1016/j.ttbdis.2022.102025
865 Esteves, E., Maruyama, S. R., Kawahara, R., Fujita, A., Martins, L. A., Righi, A. A., Costa, F. B.,
866 Palmisano, G., Labruna, M. B., Sá-Nunes, A., Ribeiro, J. M. C., & Fogaça, A. C. (2017).
867 Analysis of the salivary gland transcriptome of unfed and partially fed *Amblyomma sculptum*
868 ticks and descriptive proteome of the saliva. *Frontiers in Cellular and Infection Microbiology*,
869 *7*, 476. https://doi.org/10.3389/fcimb.2017.00476

870 Eyerich, S., Eyerich, K., Traidl-Hoffmann, C., & Biedermann, T. (2018). Cutaneous barriers and
871 skin immunity: differentiating a connected network. *Trends Immunol*, *39* (4), 315-327.
872 https://doi.org/10.1016/j.it.2018.02.004
873 Finak, G., McDavid, A., Yajima, M., Deng, J., Gersuk, V., Shalek, A. K., Slichter, C. K., Miller, H.
874 W., McElrath, M. J., Prlic, M., Linsley, P. S., & Gottardo, R. (2015). MAST: a flexible statistical
875 framework for assessing transcriptional changes and characterizing heterogeneity in single-
876 cell RNA sequencing data. *Genome Biol*, *16*, 278. https://doi.org/10.1186/s13059-015-0844-5
877 Francischetti, I. M., Sa-Nunes, A., Mans, B. J., Santos, I. M., & Ribeiro, J. M. (2009). The role of
878 saliva in tick feeding. *Front Biosci*, *14* (6), 2051-2088. https://doi.org/10.2741/3363
879 Fuchs, E. (1993). Epidermal differentiation and keratin gene expression. *Journal of Cell*
880 *Science*, *1993*, 197-208. https://doi.org/10.1242/jcs.1993.Supplement_17.28
881 Girardi, M., Oppenheim, D. E., Steele, C. R., Lewis, J. M., Glusac, E., Filler, R., Hobby, P.,
882 Sutton, B., Tigelaar, R. E., & Hayday, A. C. (2001). Regulation of cutaneous malignancy by
883 γδ T cells. *Science*, *294* (5542), 605-609. https://doi.org/doi:10.1126/science.1063916
884 Glatz, M., Means, T., Haas, J., Steere, A. C., & Mullegger, R. R. (2017). Characterization of the
885 early local immune response to *Ixodes ricinus* tick bites in human skin. *Exp Dermatol*, *26* (3),
886 263-269. https://doi.org/10.1111/exd.13207
887 Hajnicka, V., Vancova-Stibraniova, I., Slovak, M., Kocakova, P., & Nuttall, P. A. (2011). Ixodid
888 tick salivary gland products target host wound healing growth factors. *Int J Parasitol*, *41* (2),
889 213-223. https://doi.org/10.1016/j.ijpara.2010.09.005
890 Havran, W. L., Chien, Y. H., & Allison, J. P. (1991). Recognition of self antigens by skin-derived T
891 cells with invariant gamma delta antigen receptors. *Science*, *252* (5011), 1430-1432.
892 https://doi.org/10.1126/science.1828619
893 Jameson, J., Ugarte, K., Chen, N., Yachi, P., Fuchs, E., Boismenu, R., & Havran, W. L. (2002). A
894 role for skin gammadelta T cells in wound repair. *Science*, *296* (5568), 747-749.
895 https://doi.org/10.1126/science.1069639

Jameson, J. M., Cauvi, G., Witherden, D. A., & Havran, W. L. (2004). A keratinocyte-responsive γδ TCR is necessary for dendritic epidermal T cell activation by damaged keratinocytes and maintenance in the epidermis. *The Journal of Immunology*, *172* (6), 3573-3579. https://doi.org/10.4049/jimmunol.172.6.3573

Jochum, W., Passegué, E., & Wagner, E. F. (2001). AP-1 in mouse development and tumorigenesis. *Oncogene*, *20* (19), 2401-2412. https://doi.org/10.1038/sj.onc.1204389

Joost, S., Annusver, K., Jacob, T., Sun, X., Dalessandri, T., Sivan, U., Sequeira, I., Sandberg, R., & Kasper, M. (2020). The molecular anatomy of mouse skin during hair growth and rest. *Cell Stem Cell*, *26* (3), 441-457.e447. https://doi.org/10.1016/j.stem.2020.01.012

Joost, S., Jacob, T., Sun, X., Annusver, K., La Manno, G., Sur, I., & Kasper, M. (2018). Single-cell transcriptomics of traced epidermal and hair follicle stem cells reveals rapid adaptations during wound healing. *Cell Rep*, *25* (3), 585-597.e587. https://doi.org/10.1016/j.celrep.2018.09.059

Joost, S., Zeisel, A., Jacob, T., Sun, X., La Manno, G., Lönnerberg, P., Linnarsson, S., & Kasper, M. (2016). Single-cell transcriptomics reveals that differentiation and spatial signatures shape epidermal and hair follicle heterogeneity. *Cell Syst*, *3* (3), 221-237.e229. https://doi.org/10.1016/j.cels.2016.08.010

Kabashima, K., Honda, T., Ginhoux, F., & Egawa, G. (2019). The immunological anatomy of the skin. *Nature Reviews Immunology*, *19* (1), 19-30. https://doi.org/10.1038/s41577-018-0084-5

Karim, S., & Ribeiro, J. M. (2015). An insight into the sialome of the lone star tick, *Amblyomma americanum*, with a glimpse on its time dependent gene expression. *PLoS One*, *10* (7), e0131292. https://doi.org/10.1371/journal.pone.0131292

Kazimirova, M., & Stibraniova, I. (2013). Tick salivary compounds: their role in modulation of host defences and pathogen transmission. *Front Cell Infect Microbiol*, *3*, 43. https://doi.org/10.3389/fcimb.2013.00043

Keyes, B. E., Liu, S., Asare, A., Naik, S., Levorse, J., Polak, L., Lu, C. P., Nikolova, M., Pasolli, H. A., & Fuchs, E. (2016). Impaired epidermal to dendritic T cell signaling slows wound repair in aged skin. *Cell*, *167* (5), 1323-1338.e1314. https://doi.org/10.1016/j.cell.2016.10.052

Kotal, J., Langhansova, H., Lieskovska, J., Andersen, J. F., Francischetti, I. M., Chavakis, T., Kopecky, J., Pedra, J. H., Kotsyfakis, M., & Chmelar, J. (2015). Modulation of host immunity by tick saliva. *J Proteomics*, *128*, 58-68. https://doi.org/10.1016/j.jprot.2015.07.005

Kotsyfakis, M., Horka, H., Salat, J., & Andersen, J. F. (2010). The crystal structures of two salivary cystatins from the tick *Ixodes scapularis* and the effect of these inhibitors on the establishment of *Borrelia burgdorferi* infection in a murine model. *Mol Microbiol*, *77* (2), 456-470. https://doi.org/10.1111/j.1365-2958.2010.07220.x

Kotsyfakis, M., Karim, S., Andersen, J. F., Mather, T. N., & Ribeiro, J. M. (2007). Selective cysteine protease inhibition contributes to blood-feeding success of the tick *Ixodes scapularis*. *J Biol Chem*, *282* (40), 29256-29263. https://doi.org/10.1074/jbc.M703143200

Kramer, C. D., Poole, N. M., Coons, L. B., & Cole, J. A. (2011). Tick saliva regulates migration, phagocytosis, and gene expression in the macrophage-like cell line, IC-21. *Exp Parasitol*, *127*(3), 665-671. https://doi.org/10.1016/j.exppara.2010.11.012

Lewis, J. M., Girardi, M., Roberts, S. J., Barbee, S. D., Hayday, A. C., & Tigelaar, R. E. (2006). Selection of the cutaneous intraepithelial gammadelta+ T cell repertoire by a thymic stromal determinant. *Nat Immunol*, *7* (8), 843-850. https://doi.org/10.1038/ni1363

Li, G., Gustafson-Brown, C., Hanks, S. K., Nason, K., Arbeit, J. M., Pogliano, K., Wisdom, R. M., & Johnson, R. S. (2003). c-Jun is essential for organization of the epidermal leading edge. *Dev Cell*, *4* (6), 865-877. https://doi.org/10.1016/s1534-5807(03)00159-x

Lun, A. T., Bach, K., & Marioni, J. C. (2016). Pooling across cells to normalize single-cell RNA sequencing data with many zero counts. *Genome Biol*, *17*, 75. https://doi.org/10.1186/s13059-016-0947-7

946 Lun, A. T., McCarthy, D. J., & Marioni, J. C. (2016). A step-by-step workflow for low-level
947 analysis of single-cell RNA-seq data with Bioconductor. *F1000Res*, *5*, 2122.
948 https://doi.org/10.12688/f1000research.9501.2
949 Macleod, A. S., & Havran, W. L. (2011). Functions of skin-resident γδ T cells. *Cell Mol Life Sci*,
950 *68* (14), 2399-2408. https://doi.org/10.1007/s00018-011-0702-x
951 Matsuura-Hachiya, Y., Arai, K. Y., Muraguchi, T., Sasaki, T., & Nishiyama, T. (2018). Type IV
952 collagen aggregates promote keratinocyte proliferation and formation of epidermal layer in
953 human skin equivalents. *Exp Dermatol*, *27* (5), 443-448. https://doi.org/10.1111/exd.13328
954 McGinnis, C. S., Murrow, L. M., & Gartner, Z. J. (2019). DoubletFinder: doublet detection in
955 single-cell RNA sequencing data using artificial nearest neighbors. *Cell Syst*, *8*(4), 329-337
956 e324. https://doi.org/10.1016/j.cels.2019.03.003
957 Misiura, M., Baszanowska, W., Ościłowska, I., Pałka, J., & Miltyk, W. (2020). Prolidase
958 stimulates proliferation and migration through activation of the PI3K/Akt/mTOR signaling
959 pathway in human keratinocytes. *Int J Mol Sci*, *21* (23), 9243.
960 https://doi.org/10.3390/ijms21239243
961 Ni, X., & Lai, Y. (2020). Keratinocyte: a trigger or an executor of psoriasis? *J Leukoc Biol*, *108*
962 (2), 485-491. https://doi.org/10.1002/JLB.5MR0120-439R
963 Nielsen, M. M., Witherden, D. A., & Havran, W. L. (2017). γδ T cells in homeostasis and host
964 defence of epithelial barrier tissues. *Nat Rev Immunol*, *17* (12), 733-745.
965 https://doi.org/10.1038/nri.2017.101
966 Oliva Chávez, A. S., Wang, X., Marnin, L., Archer, N. K., Hammond, H. L., Carroll, E. E. M.,
967 Shaw, D. K., Tully, B. G., Buskirk, A. D., Ford, S. L., Butler, L. R., Shahi, P., Morozova, K.,
968 Clement, C. C., Lawres, L., Neal, A. J. O., Mamoun, C. B., Mason, K. L., Hobbs, B.
969 E.,…Pedra, J. H. F. (2021). Tick extracellular vesicles enable arthropod feeding and promote
970 distinct outcomes of bacterial infection. *Nature Communications*, *12*(1), 3696.
971 https://doi.org/10.1038/s41467-021-23900-8

Park, S., Gonzalez, D. G., Guirao, B., Boucher, J. D., Cockburn, K., Marsh, E. D., Mesa, K. R., Brown, S., Rompolas, P., Haberman, A. M., Bellaiche, Y., & Greco, V. (2017). Tissue-scale coordination of cellular behaviour promotes epidermal wound repair in live mice. *Nat Cell Biol*, *19*(2), 155-163. https://doi.org/10.1038/ncb3472

Park, S., Matte-Martone, C., Gonzalez, D. G., Lathrop, E. A., May, D. P., Pineda, C. M., Moore, J. L., Boucher, J. D., Marsh, E., Schmitter-Sanchez, A., Cockburn, K., Markova, O., Bellaiche, Y., & Greco, V. (2021). Skin-resident immune cells actively coordinate their distribution with epidermal cells during homeostasis. *Nat Cell Biol*, *23* (5), 476-484. https://doi.org/10.1038/s41556-021-00670-5

Pastar, I., Stojadinovic, O., Yin, N. C., Ramirez, H., Nusbaum, A. G., Sawaya, A., Patel, S. B., Khalid, L., Isseroff, R. R., & Tomic-Canic, M. (2014). Epithelialization in wound healing: a comprehensive review. *Adv Wound Care 3* (7), 445-464. https://doi.org/10.1089/wound.2013.0473

Peña, O. A., & Martin, P. (2024). Cellular and molecular mechanisms of skin wound healing. *Nature Reviews Molecular Cell Biology 25 (8)*, 599-616. https://doi.org/10.1038/s41580-024-00715-1

Piipponen, M., Li, D., & Landén, N. X. (2020). The immune functions of keratinocytes in skin wound healing. *Int J Mol Sci*, *21* (22), 8790. https://doi.org/10.3390/ijms21228790

Poole, N. M., Mamidanna, G., Smith, R. A., Coons, L. B., & Cole, J. A. (2013). Prostaglandin E_2 in tick saliva regulates macrophage cell migration and cytokine profile. *Parasites & Vectors*, *6* (1), 261. https://doi.org/10.1186/1756-3305-6-261

Proksch, E., Brandner, J. M., & Jensen, J.-M. (2008). The skin: an indispensable barrier. *Experimental Dermatology*, *17* (12), 1063-1072. https://doi.org/https://doi.org/10.1111/j.1600-0625.2008.00786.x

Ribeiro, J. M., Evans, P. M., MacSwain, J. L., & Sauer, J. (1992). *Amblyomma americanum*: characterization of salivary prostaglandins E_2 and F_2 alpha by RP-HPLC/bioassay and gas

chromatography-mass spectrometry. *Exp Parasitol*, *74* (1), 112-116. https://doi.org/10.1016/0014-4894(92)90145-z

Ribeiro, J. M., Makoul, G. T., Levine, J., Robinson, D. R., & Spielman, A. (1985). Antihemostatic, antiinflammatory, and immunosuppressive properties of the saliva of a tick, *Ixodes dammini*. *J Exp Med*, *161* (2), 332-344. https://doi.org/10.1084/jem.161.2.332

Ribeiro, J. M., Makoul, G. T., & Robinson, D. R. (1988). *Ixodes dammini*: evidence for salivary prostacyclin secretion. *J Parasitol*, *74* (6), 1068-1069.

Rice, G., & Rompolas, P. (2020). Advances in resolving the heterogeneity and dynamics of keratinocyte differentiation. *Curr Opin Cell Biol*, *67*, 92-98. https://doi.org/10.1016/j.ceb.2020.09.004

Rosenberg, R., Lindsey, N. P., Fischer, M., Gregory, C. J., Hinckley, A. F., Mead, P. S., Paz-Bailey, G., Waterman, S. H., Drexler, N. A., Kersh, G. J., Hooks, H., Partridge, S. K., Visser, S. N., Beard, C. B., & Petersen, L. R. (2018). Vital signs: trends in reported vectorborne disease cases - United States and Territories, 2004-2016. *MMWR Morb Mortal Wkly Rep*, *67*(17), 496-501. https://doi.org/10.15585/mmwr.mm6717e1

Rousselle, P., Braye, F., & Dayan, G. (2019). Re-epithelialization of adult skin wounds: cellular mechanisms and therapeutic strategies. *Adv Drug Deliv Rev*, *146*, 344-365. https://doi.org/10.1016/j.addr.2018.06.019

Schmierer, B., & Hill, C. S. (2007). TGFβ–SMAD signal transduction: molecular specificity and functional flexibility. *Nature Reviews Molecular Cell Biology*, *8*(12), 970-982. https://doi.org/10.1038/nrm2297

Schoeler, G. B., Manweiler, S. A., & Wikel, S. K. (1999). *Ixodes scapularis*: effects of repeated infestations with pathogen-free nymphs on macrophage and T lymphocyte cytokine responses of BALB/c and C3H/HeN mice. *Exp Parasitol*, *92*(4), 239-248. https://doi.org/10.1006/expr.1999.4426

1023 Sellheyer, K., Bickenbach, J. R., Rothnagel, J. A., Bundman, D., Longley, M. A., Krieg, T.,
1024 Roche, N. S., Roberts, A. B., & Roop, D. R. (1993). Inhibition of skin development by
1025 overexpression of transforming growth factor beta 1 in the epidermis of transgenic mice. *Proc*
1026 *Natl Acad Sci U S A*, *90* (11), 5237-5241. https://doi.org/10.1073/pnas.90.11.5237
1027 Sharma, A., Pham, M. N., Reyes, J. B., Chana, R., Yim, W. C., Heu, C. C., Kim, D., Chaverra-
1028 Rodriguez, D., Rasgon, J. L., Harrell, R. A., 2nd, Nuss, A. B., & Gulia-Nuss, M. (2022). Cas9-
1029 mediated gene editing in the black-legged tick, *Ixodes scapularis*, by embryo injection and
1030 ReMOT Control. *iScience*, *25* (3), 103781. https://doi.org/10.1016/j.isci.2022.103781
1031 Sharp, L. L., Jameson, J. M., Cauvi, G., & Havran, W. L. (2005). Dendritic epidermal T cells
1032 regulate skin homeostasis through local production of insulin-like growth factor 1. *Nat*
1033 *Immunol*, *6* (1), 73-79. https://doi.org/10.1038/ni1152
1034 Simo, L., Kazimirova, M., Richardson, J., & Bonnet, S. I. (2017). The essential role of tick
1035 salivary glands and saliva in tick feeding and pathogen transmission. *Front Cell Infect*
1036 *Microbiol*, *7*, 281. https://doi.org/10.3389/fcimb.2017.00281
1037 Singer, A. J., & Clark, R. A. F. (1999). Cutaneous wound healing. *New England Journal of*
1038 *Medicine*, *341* (10), 738-746. https://doi.org/10.1056/nejm199909023411006
1039 Sonenshine, D. E., & Roe, R. M. (2014). *Biology of Ticks* (Vol. 1). Oxford University Press.
1040 Street, K., Risso, D., Fletcher, R. B., Das, D., Ngai, J., Yosef, N., Purdom, E., & Dudoit, S.
1041 (2018). Slingshot: cell lineage and pseudotime inference for single-cell transcriptomics. *BMC*
1042 *Genomics*, *19* (1), 477. https://doi.org/10.1186/s12864-018-4772-0
1043 Tanner, S. M., & Lorenz, R. G. (2022). FVB/N mouse strain regulatory T cells differ in phenotype
1044 and function from the C57BL/6 and BALB/C strains. *FASEB Bioadv*, *4*(10), 648-661.
1045 https://doi.org/10.1096/fba.2021-00161
1046 Thelen, F., & Witherden, D. A. (2020). Get in touch with dendritic epithelial T cells! *Front*
1047 *Immunol*, *11*, 1656. https://doi.org/10.3389/fimmu.2020.01656

1048 Valenzuela, J. G., Francischetti, I. M. B., Pham, V. M., Garfield, M. K., Mather, T. N., & Ribeiro,
1049 J. M. C. (2002). Exploring the sialome of the tick *Ixodes scapularis*. *Journal of Experimental*
1050 *Biology*, *205* (18), 2843-2864. https://doi.org/10.1242/jeb.205.18.2843
1051 Whang, M. I., Guerra, N., & Raulet, D. H. (2009). Costimulation of dendritic epidermal
1052 gammadelta T cells by a new NKG2D ligand expressed specifically in the skin. *J Immunol*,
1053 *182*(8), 4557-4564. https://doi.org/10.4049/jimmunol.0802439
1054 Wikel, S. (2013). Ticks and tick-borne pathogens at the cutaneous interface: host defenses, tick
1055 countermeasures, and a suitable environment for pathogen establishment. *Front Microbiol*, *4*,
1056 337. https://doi.org/10.3389/fmicb.2013.00337
1057 Wikramanayake, T. C., Stojadinovic, O., & Tomic-Canic, M. (2014). Epidermal differentiation in
1058 barrier maintenance and wound Healing. *Adv Wound Care*, *3*(3), 272-280.
1059 https://doi.org/10.1089/wound.2013.0503
1060 Witherden, Deborah A., Watanabe, M., Garijo, O., Rieder, Stephanie E., Sarkisyan, G., Cronin,
1061 Shane J. F., Verdino, P., Wilson, Ian A., Kumanogoh, A., Kikutani, H., Teyton, L., Fischer,
1062 Wolfgang H., & Havran, Wendy L. (2012). The CD100 receptor interacts with its plexin B2
1063 ligand to regulate epidermal γδ T cell function. *Immunity*, *37* (2), 314-325.
1064 https://doi.org/https://doi.org/10.1016/j.immuni.2012.05.026
1065 Woodworth, C. D., Michael, E., Smith, L., Vijayachandra, K., Glick, A., Hennings, H., & Yuspa,
1066 S. H. (2004). Strain-dependent differences in malignant conversion of mouse skin tumors is
1067 an inherent property of the epidermal keratinocyte. *Carcinogenesis*, *25* (9), 1771-1778.
1068 https://doi.org/10.1093/carcin/bgh170

1069

Supplementary Table 1: Primers and siRNA sequences

Target	Type	Location Within mRNA	SiRNA/Primer Name	Strand	Primer Sequence
I. scapularis Vamp33	siRNA	Start at 300	Vamp33SiF	Forward	AAGGACACAGTGTGGAGAGATCCTGTCTC
			Vamp33SiR	Reverse	AAATCTCTCCACACTGTGTCCCCTGTCTC
	Scrambled		Vamp33ScF	Forward	AAGTGAGGGACGCATAGTAGACCTGTCTC
			Vamp33ScR	Reverse	AATCTACTATGCGTCCCTCACCCTGTCTC
	qRT-PCR	Start at 76	Vamp33qR-F	Forward	TCATACCTGAAGTTGTCCAA
		Start at 180	Vamp33qR-R	Reverse	CTCAAGAATGCCACTGTTG
D. variabilis Vamp33	siRNA	Start at 280	Vamp33Derm-SiF	Forward	AACCGGATGGTGATGTTAATCCCTGTCTC
			Vamp33Derm-SiR	Reverse	AAGATTAACATCACCATCCGGCCTGTCTC
	Scrambled		Vamp33Derm-ScF	Forward	AAGCCTCAGGTGGAATTAGTTCCTGTCTC
			Vamp33Derm-ScR	Reverse	AAAACTAATTCCACCTGAGGCCCTGTCTC
	qRT-PCR	Start at 78	Vamp33DqR-2F	Forward	TCACCTAAAGTTGTCCAACCC
		Start at 160	Vamp33DqR-2R	Reverse	TCAAGGATTCCACTGTTGGG
	qRT-PCR	Start at 64	Vamp33DqR-F	Forward	GACGTGGTTACTTCTCACCTAAA
		Start at 148	Vamp33DqR-R	Reverse	CTGTTGGGCCGTACACAATA
A. americanum Vamp33	siRNA	Start at 280	Vamp33AA-SiF	Forward	AACCAGATGGTGATGTGAACCCCTGTCTC
			Vamp33AA-SiR	Reverse	AAGGTTCACATCACCATCTGGCCTGTCTC
	Scrambled		Vamp33AA-ScF	Forward	AAGGGTGCTAACACGGACTTACCTGTCTC
			Vamp33AA-ScR	Reverse	AATAAGTCCGTGTTAGCACCCCCTGTCTC
	qRT-PCR	Start at 76	Vamp33AA qR-F	Forward	TCTCATCTAAAGCTTTCCAACCC
		Start at 160	Vamp33AA qR-R	Reverse	AAGGATGCCACTGTTGGG
I. scapularis β-actin	qRT-PCR	Start at 618	ActinIS 2F	Forward	GGTCATCACAATCGGCAAC
		Start at 742	ActinIS *2*R	Reverse	ATGGAGTTGTACGTGGTCTC
A. americanum β-actin	qRT-PCR	Start at 285	ActinAA F	Forward	GTCATGGTCGGCATGGG
		Start at 365	ActinAA R	Reverse	ATGCCGTGCTCAATGGG
D. variabilis β-actin	qRT-PCR	Start at 798	ActinIS 2F	Forward	GGTCATCACAATCGGCAAC
		Start at 905	ActinIS *2*R	Reverse	ATGGAGTTGTACGTGGTCTC

Supplementary Table 2: Cell markers

Cell type	Cell population	Gene	Ensembl
Antigen presenting cells	All	*H2-Aa*	ENSMUSG00000036594
		H2-Ab1	ENSMUSG00000073421
	Langerhans	*Cd207*	ENSMUSG00000034783
	Dendritic cells	*Itgax*	ENSMUSG00000030789
		Cd80	ENSMUSG00000075122
		Cd86	ENSMUSG00000022901
		Ly75	ENSMUSG00000026980
		Cd209a	ENSMUSG00000031494
	Macrophage	*Adgre1*	ENSMUSG00000004730
		Itgam	ENSMUSG00000030786
Keratinocytes	Undifferentiated (Stratum basale)	*Krt5*	ENSMUSG00000061527
		Krt14	ENSMUSG00000045545
		Krt15	ENSMUSG00000054146
	Differentiating (Stratum spinosum)	*Krt 1*	ENSMUSG00000046834
		Krt2	ENSMUSG00000064201
		Krt10	ENSMUSG00000019761
	Terminally differentiated (Stratum granulosum)	*Ivl*	ENSMUSG00000049128
		Flg	ENSMUSG00000102439
	Corneocytes (Stratum corneum)	*Klk5*	ENSMUSG00000074155
T cells	All	*Cd3d*	ENSMUSG00000032094
		Cd3e	ENSMUSG00000032093
		Cd3g	ENSMUSG00000002033
	αβ T cell	*Trac*	ENSMUSG00000076928
		Trbc1	ENSMUSG00000076490

		Trbc2	ENSMUSG00000076498
		CD4	ENSMUSG00000023274
		CD8a	ENSMUSG00000053977
	γδ T cell	*Trdc*	ENSMUSG00000104876
		Tcrg-C1	ENSMUSG00000076749
		Tcrg-C2	ENSMUSG00000076752
		Tcrg-C4	ENSMUSG00000076757
	DETCs	*Trdv4*	ENSMUSG00000076867
		Sema4d	ENSMUSG00000021451
		Jaml	ENSMUSG00000048534
		Klrk1	ENSMUSG00000030149
Endothelial		*Cldn5*	ENSMUSG00000041378
		Cdh5	ENSMUSG00000031871
		Egfl7	ENSMUSG00000026921
Fibroblasts		*Dcn*	ENSMUSG00000019929
		Fgf2	ENSMUSG00000037225
		Fgf7	ENSMUSG00000027208
Hair follicle	Upper hair follicle	*Krt79*	ENSMUSG00000061397
		Krt17	ENSMUSG00000035557
	Sebaceous gland	*Mgst1*	ENSMUSG00000008540
		Scd1	ENSMUSG00000037071
	Outer bulge	*Postn*	ENSMUSG00000027750
		Lgr5	ENSMUSG00000020140
	Inner bulge	*Krt6a*	ENSMUSG00000058354
		Krt75	ENSMUSG00000022986
	Base of follicle	*Shh*	ENSMUSG00000002633
	Hair germ	*Gli1*	ENSMUSG00000025407
Melanocytes		*Dct*	ENSMUSG00000022129

		Mlana	ENSMUSG00000024806
		Tyr	ENSMUSG00000004651
Red blood cells		*Hbb-bs*	ENSMUSG00000052305
		Hbb-bt	ENSMUSG00000073940
Schwann cells		*Mal*	ENSMUSG00000027375
		Plp1	ENSMUSG00000031425
		Sox10	ENSMUSG00000033006
Smooth muscle cells		*Acta2*	ENSMUSG00000035783
		Myh11	ENSMUSG00000018830
		Myl9	ENSMUSG00000067818
		Myocd	ENSMUSG00000067818
		Rgs5	ENSMUSG00000026678

1073

Supplementary Table 3: Resources and reagents available

Antibody	Source	Identifier	Dilution/ Concentration
7-AAD Viability Staining Solution	Biolegend	420404	1:500
Zombie Violet Fixable Live Dead stain	Biolegend	423113	1:500
Zombie NIR Fixable Live Dead stain	Biolegend	423105	1:500
Anti-mouse CD16/32 Antibody	Biolegend	156603	1:500
APC anti-mouse CD45 Antibody clone: 30-F11	Biolegend	103111	1:100
FITC anti-mouse CD3 Antibody clone:17A2	Biolegend	100203	1:100
BV650 anti-mouse Vy3 Antibody clone: 536	BD	743241	1:50
PE Mouse Anti-Rat IgM clone:G53-238	BD	553888	1:100
Monoclonal antibody 17D1	Adrian Hayday, Kings College London and Robert Tigelaar, Yale University	N/A	1:50
PE/Cyanine7 anti-mouse CD45 Antibody clone: 30-F11	Biolegend	103114	1:100
APC anti-mouse Thy1.2 Antibody clone: 30-H12	Biolegend	105312	1:100
PE anti-mouse JAML Antibody clone: 4E10	Biolegend	128503	1:100
BV711 anti-mouse CD100 Antibody clone: BMA-12	BD	745492	1:100
PE/Cyanine5 anti-mouse CD44 Antibody clone: IM7	Biolegend	103010	1:100
APC/Cyanine7 anti-mouse CD25 Antibody clone: PC61	Biolegend	102026	1:100
PerCP/Cyanine5.5 anti-mouse CD69 Antibody clone: H1.2F3	Biolegend	104522	1:100
APC anti-mouse CD314 (NKG2D) Antibody clone: CX5	Biolegend	130212	1:100
Alexa Fluor 700 anti-mouse Ki-67 Antibody clone: 16A8	Biolegend	652420	1:50
BV711 anti-mouse CD326 (Ep-CAM) Antibody clone: G8.8	Biolegend	118233	1:100
PE anti-mouse CD200 Antibody clone: OX-90	Biolegend	123807	1:100
PE/Cyanine5 anti-mouse CD34 Antibody clone: MEC14.7	Biolegend	119312	1:100
BV605 anti-mouse Sca1 Antibody clone: D7	Biolegend	108133	1:100

PE anti-mouse CD49f Antibody clone: GoH3	Biolegend	313612	1:100
FITC Phospho-PI3K p85/p55 (Tyr458, Tyr199) Monoclonal Antibody clone: PI3KY458-1A11	ThermoFisher Scientific	MA5-36955	1:50
PI3K p85α Monoclonal Antibody clone: SU04-07	ThermoFisher Scientific	MA5-41128	1:50
Alexa Fluor 405 Goat anti-Rabbit IgG (H+L) Secondary Antibody	ThermoFisher Scientific	A-31556	1:100
Anti-MADH7/SMAD7 polyclonal antibody	Abcam	ab216428	1:100

Cell media			
Leibovitz's L-15 Medium, powder	Gibco	41300039	N/A
L-aspartic acid	Millipore-Sigma	11189	0.449 g/L
L-glutamine	Millipore-Sigma	G8540	0.500 g/L
L-proline	Millipore-Sigma	81709	0.450 g/L
L-glutamic acid	Millipore-Sigma	49449	0.250 g/L
α-ketoglutaric acid	Millipore-Sigma	K1128	0.449 g/L
Sodium hydroxide	Millipore-Sigma	S8045	10 N
D-glucose	Millipore-Sigma	G7021	18.018 g/L
FBS (USDA approved; for tick media)	Millipore-Sigma	F0926-500ML	0.1
Bacto™ Tryptose Phophate Broth	BD	260300	5%
Lipoprotein Concentrate	MP Biomedicals	191476	0.1%
Corning® 100 mL Penicillin-Streptomycin Solution, 100x	Corning	30-002-CI	1:100
Amphotericin B	Gibco	15290-026	1:100
Distilled water	Gibco	15-230-147	N/A
Materials			
Cell culture plate with lid (6 well, flat bottom)	Sigma	SIAL0516	N/A

Cellstart®, 96 well cell culture plate, F-bottom	Greiner bio-one	655 160	N/A
Costar® cell culture plate with lid (24 well, flat bottom)	Corning	CLS3526-1EA	N/A
Nunc™ 96-Well Polystyrene Round Bottom Microwell Plates	Thermo Scientific	262162	N/A
Vannas spring scissors, 4 mm cutting edge straight	Fine Science	15018-10	N/A
Integra Miltex 2 mm biopsy punches	Integra	95039-098	N/A
Integra Miltex 5 mm biopsy punches	Integra	33-35	N/A
AcuPunch biopsy punches 10 mm	Acuderm	P1050	N/A
FALCON® 14 ml Polypropylene round-bottom tube	Corning	352059	N/A
Corning® cell strainer size 40 µm, blue, sterile	Corning	431750	N/A
Falcon 5 mL Round Bottom Polystyrene Test Tube, with Cell Strainer Snap Cap	Corning	352235	N/A
12x75mm Plastic Tubes	Globe Scientific	110441	N/A
1.5 mL Eppendorf Safe-Lock Tubes	USA Scientific	1615-5500	N/A
1.5ml Microcentrifuge Tubes with Socket Screw Caps	VWR	525-1238	N/A
Lo-bind tubes	Eppendorf	22431048	N/A
Vannas Spring Scissors - 4mm	Fine Science Tools	15018-10	N/A
Reagents			
Trypsin/Lys-C Mix, Mass Spec Grade	Promega	V5071	N/A
Bovine Serum Albumin	Millipore-Sigma	A2058-5G	N/A
BenchMark™ FBS	Gemini Bio-products	100-106	1:10
Methanol anhydrous, 99.8%	Millipore-Sigma	322415-1L	0-20%
Ethyl alconol, Pure; 200 proof for molecular biology	Millipore-Sigma	E7023-1L	1:1
TRIzol reagent	Ambion	15596018	N/A
Liberase™ TL Research Grade	Roche	5401020001	10%
RPMI-1640 with L-Glutamine	Quality Biological	722461	N/A

DNase I	Roche	11284932001	N/A
10X Phosphate-buffered saline (PBS)	Quality Biological	119-069-131	1X
Phosphate-buffered saline (PBS)	Gibco	10010-023	N/A
0.5M Ethylenediaminetetraacetic acid (EDTA), pH 8.0	Boston BioProducts	BM-150	N/A
Sodium azide (NaN3)	Sigma-Aldrich	S2002-25G	N/A
Paraformaldehyde	Thermo Fisher Scientific	J61899-AP	N/A
RIPA lysis buffer	Millipore	20-188	1X
Halt Protease Inhibitor Cocktail	Thermo Fisher Scientific	87786	1X
Halt™ Phosphatase Inhibitor Cocktail	Thermo Fisher Scientific	78420	1X
Dispase II	Sigma-Aldrich	D4693-1G	NA
Dispase	Gibco	17105-041	4 U/mL
Magnesium chloride (MgCl2)	Sigma-Aldrich	M2393-100G	5mM
Calcium chloride (CaCl2)	Sigma-Aldrich	C1016-100G	0.4mM
Collagenase D	Sigma-Aldrich	11088866001	2.5mg/mL
Gum rosin	Millipore-Sigma	60895	75% (3/4 parts)
Beeswax	Thermo Fisher Scientific	S25192A	25% (1/4 parts)
Cytochalasin D	Sigma-Aldrich	C8273	1:100
Commercial Assays			
Pure Link RNA mini kit	Ambion	12183025	N/A
Silencer™ siRNA Construction Kit	Thermo Scientific	AM1620	N/A
Verso cDNA Synthesis Kit	Thermo Scientific	AB-1453B	N/A
Pierce BCA Protein Assay Kit	Thermo Scientific	23227	N/A
DNeasy® Blood and Tissue kit	Qiagen	69506	N/A

FOXP3 Fix/Perm Buffer Set	BioLegend	421403	N/A
Human KGF/FGF-7 Quantikine ELISA Kit	R&D Systems	DKG00	NA
Human/Mouse/Rat/Porcine/Canine TGF-β 1 ELISA – Quantikine kit	R&D Systems	DB100C	NA
Organisms			
Ixodes scapularis adult partially fed female ticks	Albert Mulenga, Texas A&M University	N/A	N/A
Ixodes scapularis adult partially fed female ticks	Adela Oliva Chavez, Texas A&M University	N/A	N/A
Ixodes scapularis nymph ticks	Jon Oliver and Ulrike Munderloh, University of Minnesota	N/A	N/A
Ixodes scapularis nymph ticks	Tick Lab, Oklahoma State University	N/A	N/A
Amblyomma americanum nymph ticks	Tick Lab, Oklahoma State University	N/A	N/A
Dermacentor variabilis nymph ticks	Tick Lab, Oklahoma State University	N/A	N/A
C57BL6J (WT) mice	University of Maryland	N/A	N/A
C57BL6J (WT) mice	Jackson Laboratories	#000664	N/A
FVB/NJ mice	The Jackson Laboratory	001800	N/A
FVB/NTac mice	Taconic Biosciences	N/A	N/A
Equipment			
CFX96 Touch Real-Time PCR Detection System	Biorad	N/A	N/A
Nanoject III	Drummond Scientific Company	3-000-207	N/A
NanoSight NS300	Malvern Panalytical	N/A	N/A
Percival I30BLL incubator	Percival	I30BLL	N/A
Software			
GraphPad Prism v9.1.2	https://www.graphpad.com/	N/A	N/A
GraphPad Quick Cals Outlier Calculator	https://www.graphpad.com/quickcalcs/Grubbs1.cfm	N/A	N/A

FlowJo (v10.6.1 – 10.8.1)	https://www.flowjo.com/	N/A	N/A
QIAGEN Ingenuity Pathway Analysis	https://digitalinsights.qiagen.com/products-overview/discovery-insights-portfolio/analysis-and-visualization/qiagen-ipa/	N/A	N/A
Database for Annotation, Visualization and Integrated Discovery (DAVID) (version 2021)	https://david.ncifcrf.gov/	N/A	N/A

1075

1076

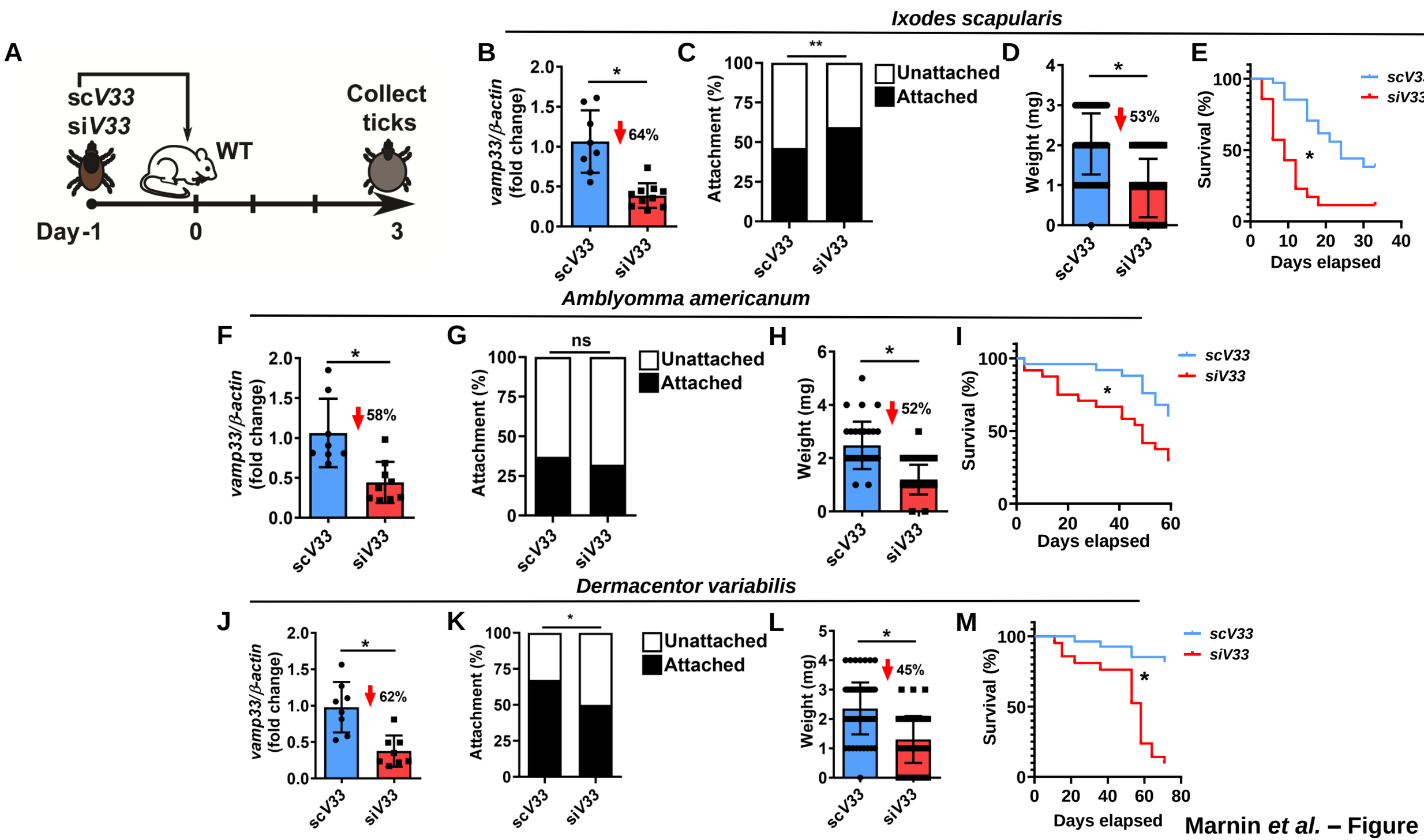

Marnin *et al.* – Figure 1

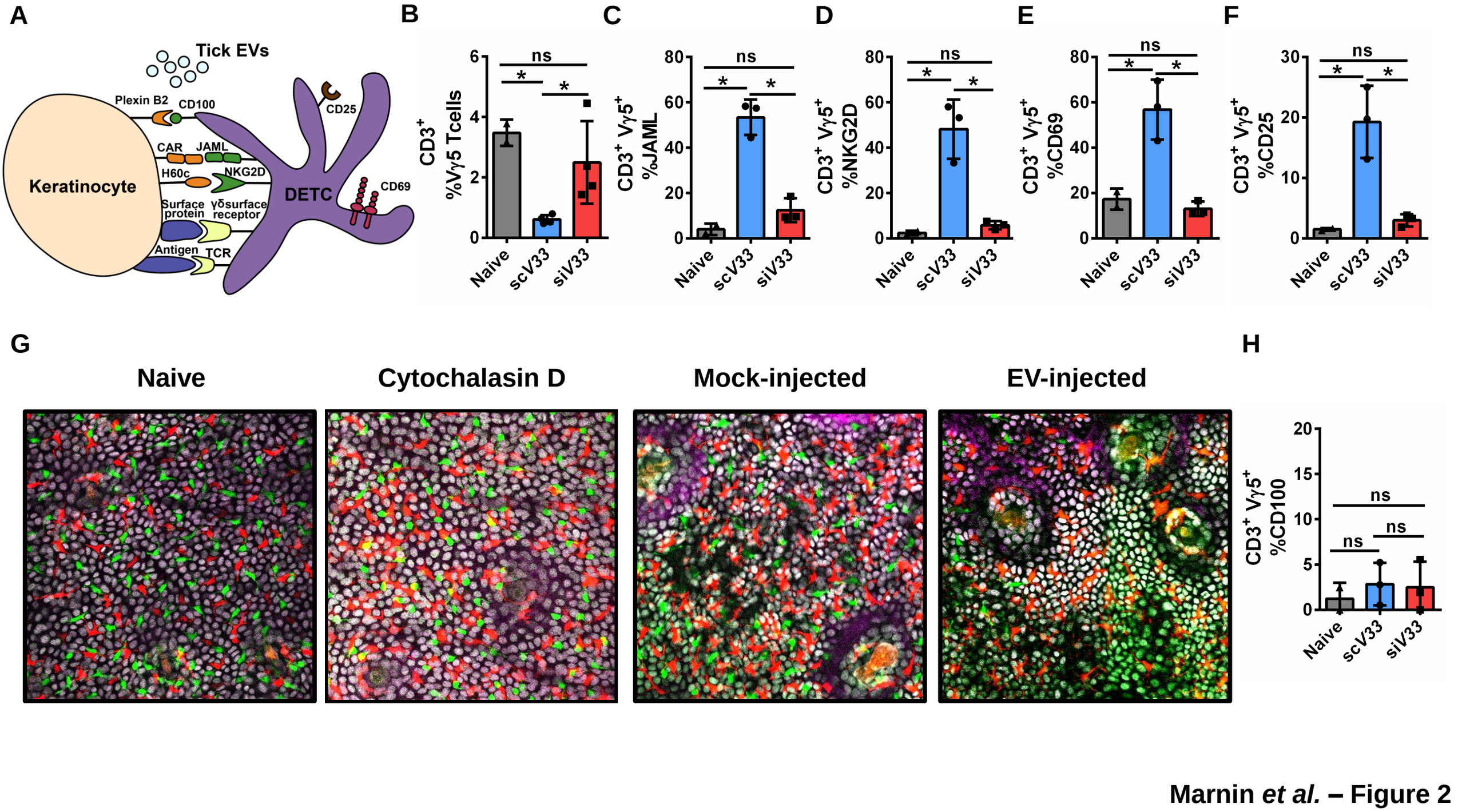

Marnin *et al.* – Figure 2

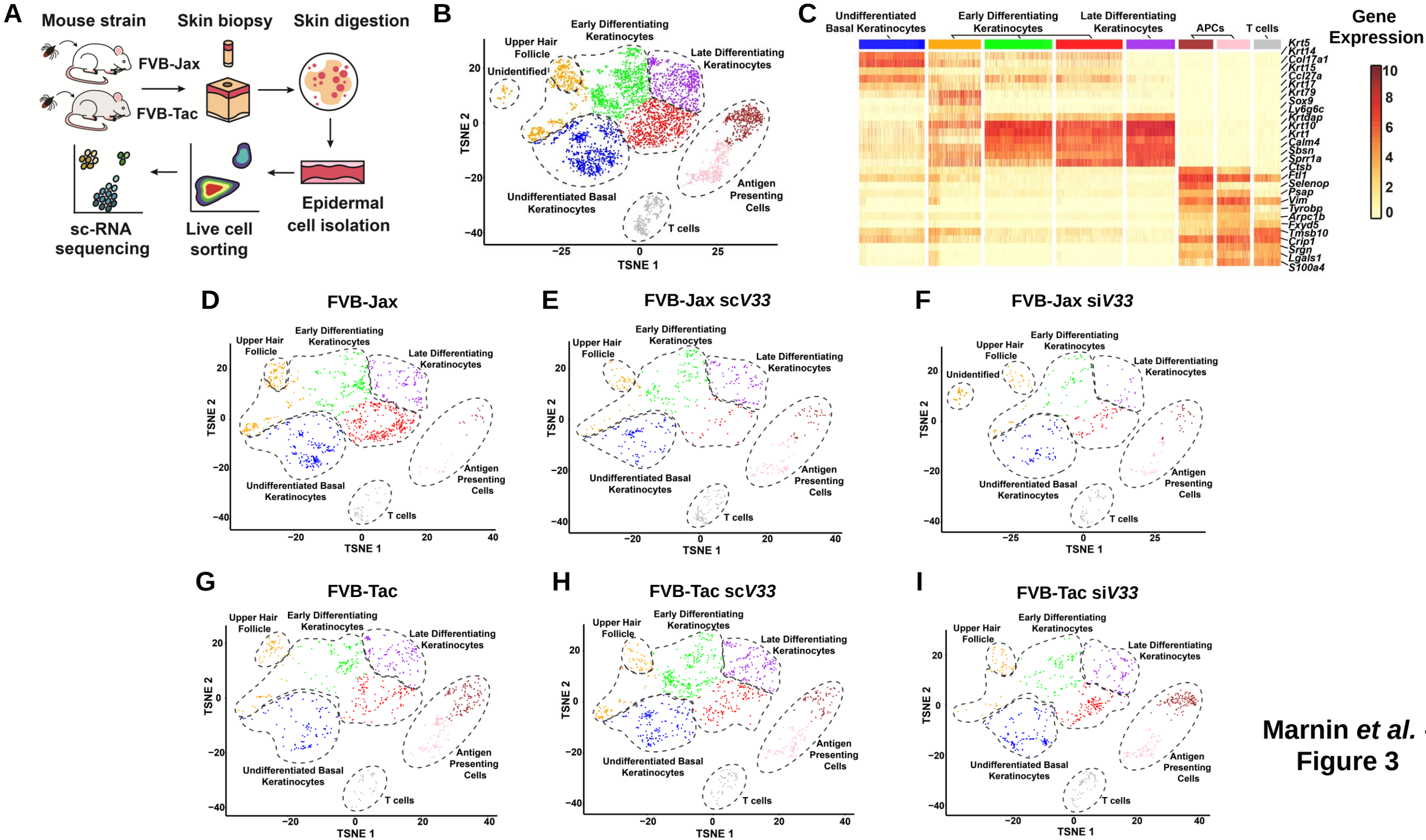

Marnin *et al.* - Figure 3

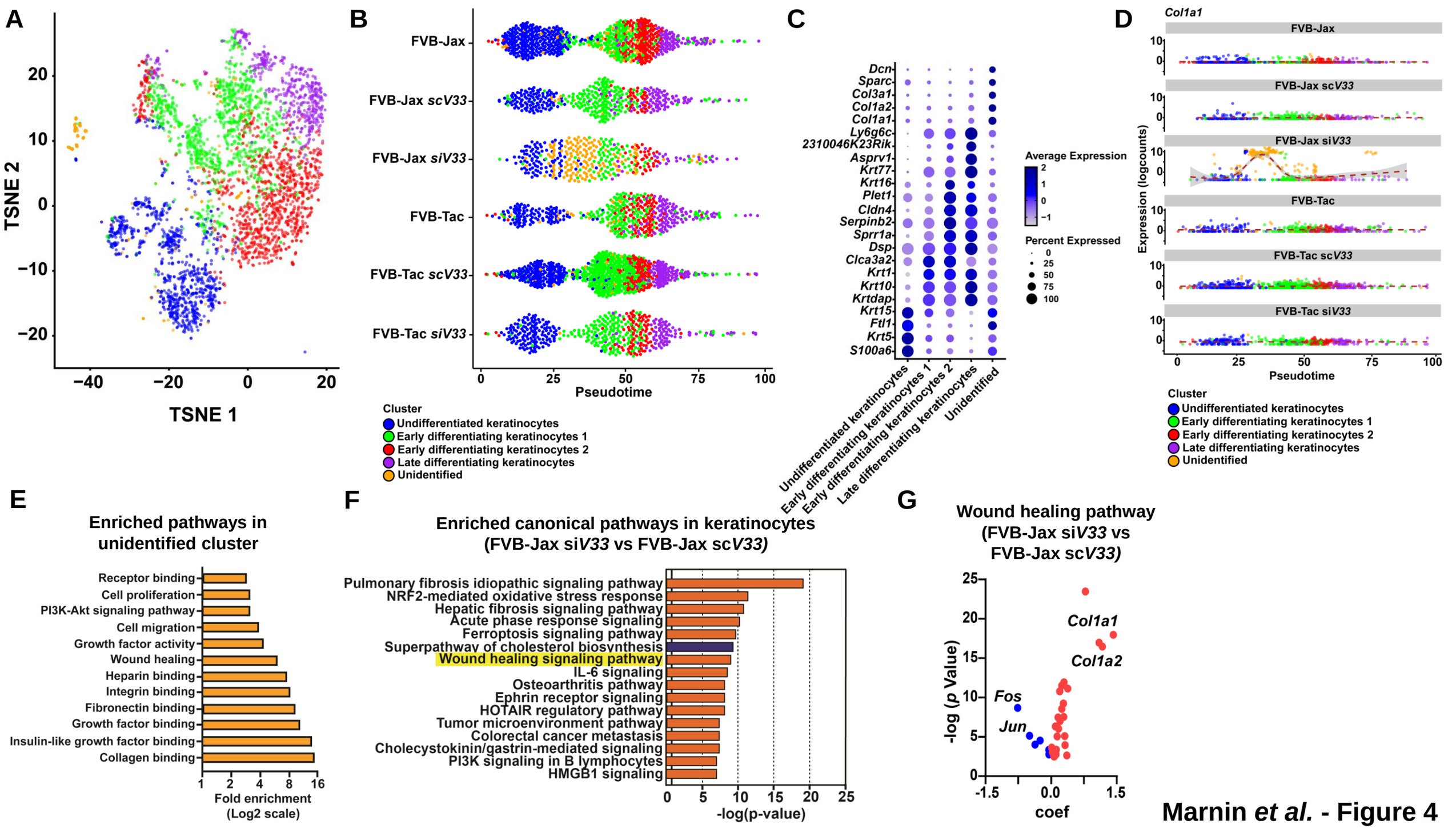
A
TSNE 2
TSNE 1
B
FVB-Jax
FVB-Jax scV33
FVB-Jax siV33
FVB-Tac
FVB-Tac scV33
FVB-Tac siV33
Pseudotime
Cluster
Undifferentiated keratinocytes
Early differentiating keratinocytes 1
Early differentiating keratinocytes 2
Late differentiating keratinocytes
Unidentified
C
Dcn
Sparc
Col3a1
Col1a2
Col1a1
Ly6g6c
2310046K23Rik
Asprv1
Krt77
Krt16
Plet1
Cldn4
Serpinb2
Sprr1a
Dsp
Clca3a2
Krt1
Krt10
Krtdap
Krt15
Ftl1
Krt5
S100a6
Average Expression
Percent Expressed
D
Col1a1
Expression (logcounts)
Pseudotime
E
Enriched pathways in unidentified cluster
Receptor binding
Cell proliferation
PI3K-Akt signaling pathway
Cell migration
Growth factor activity
Wound healing
Heparin binding
Integrin binding
Fibronectin binding
Growth factor binding
Insulin-like growth factor binding
Collagen binding
Fold enrichment (Log2 scale)
F
Enriched canonical pathways in keratinocytes (FVB-Jax siV33 vs FVB-Jax scV33)
Pulmonary fibrosis idiopathic signaling pathway
NRF2-mediated oxidative stress response
Hepatic fibrosis signaling pathway
Acute phase response signaling
Ferroptosis signaling pathway
Superpathway of cholesterol biosynthesis
Wound healing signaling pathway
IL-6 signaling
Osteoarthritis pathway
Ephrin receptor signaling
HOTAIR regulatory pathway
Tumor microenvironment pathway
Colorectal cancer metastasis
Cholecystokinin/gastrin-mediated signaling
PI3K signaling in B lymphocytes
HMGB1 signaling
-log(p-value)
G
Wound healing pathway (FVB-Jax siV33 vs FVB-Jax scV33)
-log (p Value)
Col1a1
Col1a2
Fos
Jun
coef
Marnin et al. - Figure 4

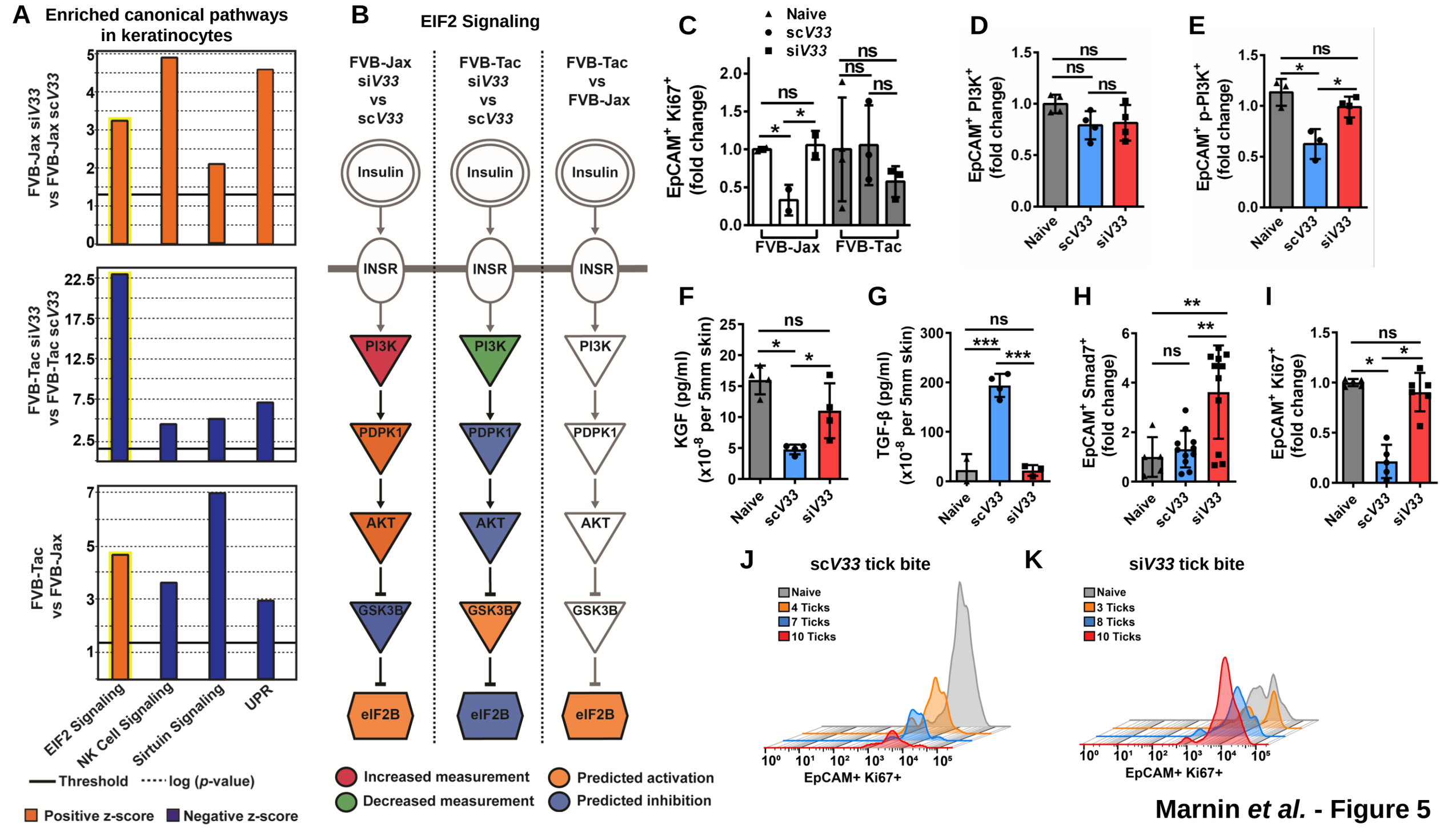

Marnin *et al.* - Figure 5